[Short title + Author Name - P&H title] 31 (2023) 101852

HOSTED BY

ELSEVIER

Contents lists available at ScienceDirect

Saudi Pharmaceutical Journal

journal homepage: www.sciencedirect.com

Computer-assisted drug discovery (CADD) of an anti-cancer derivative of the theobromine alkaloid inhibiting VEGFR-2

Ibrahim H. Eissa [a,*], Reda G. Yousef [a], Mostafa A. Asmaey [b], Hazem Elkady [a], Dalal Z. Husein [c], Aisha A. Alsfouk [d], Ibrahim M. Ibrahim [e], Mohamed A. Elkady [f], Eslam B. Elkaeed [g,*], Ahmed M. Metwaly [h,i,*]

[a] Pharmaceutical Medicinal Chemistry & Drug Design Department, Faculty of Pharmacy (Boys), Al-Azhar University, Cairo 11884, Egypt
[b] Department of Chemistry, Faculty of Science, Al-Azhar University, Assiut Branch, 71524, Assiut, Egypt
[c] Chemistry Department, Faculty of Science, New Valley University, El-Kharja 72511, Egypt
[d] Department of Pharmaceutical Sciences, College of Pharmacy, Princess Nourah bint Abdulrahman University, P.O. Box 84428, Riyadh 11671, Saudi Arabia
[e] Biophysics Department, Faculty of Science, Cairo University, Cairo 12613, Egypt
[f] Biochemistry and Molecular Biology Department, Faculty of Pharmacy (Boys), Al-Azhar University, Nasr City, Cairo 11231, Egypt
[g] Department of Pharmaceutical Sciences, College of Pharmacy, AlMaarefa University, Riyadh 13713, Saudi Arabia
[h] Pharmacognosy and Medicinal Plants Department, Faculty of Pharmacy (Boys), Al-Azhar University, Cairo 11884, Egypt
[i] Biopharmaceutical Products Research Department, Genetic Engineering and Biotechnology Research Institute, City of Scientific Research and Technological Applications (SRTA-City), Alexandria, Egypt

ARTICLE INFO

Keywords:
Theobromine derivatives
Breast cancer
VEGFR-2 inhibitors
Semi synthesis
MD simulations
Anti-proliferative
Apoptosis

ABSTRACT

VEGFR-2 is a significant target in cancer treatment, inhibiting angiogenesis and impeding tumor growth. Utilizing the essential pharmacophoric structural properties, a new semi-synthetic theobromine analogue (**T-1-MBHEPA**) was designed as VEGFR-2 inhibitor. Firstly, **T-1-MBHEPA**'s stability and reactivity were indicated through several DFT computations. Additionally, molecular docking, MD simulations, MM-GPSA, PLIP, and essential dynamics (ED) experiments suggested **T-1-MBHEPA**'s strong binding capabilities to VEGFR-2. Its computational ADMET profiles were also studied before the semi-synthesis and indicated a good degree of drug-likeness. **T-1-MBHEPA** was then semi-synthesized to evaluate the design and the *in silico* findings. It was found that, **T-1-MBHEPA** inhibited VEGFR-2 with an IC_{50} value of 0.121 ± 0.051 μM, as compared to sorafenib which had an IC_{50} value of 0.056 μM. Similarly, **T-1-MBHEPA** inhibited the proliferation of HepG2 and MCF7 cell lines with IC_{50} values of 4.61 and 4.85 μg/mL respectively - comparing sorafenib's IC_{50} values which were 2.24 μg/mL and 3.17 μg/mL respectively. Interestingly, **T-1-MBHEPA** revealed a noteworthy IC_{50} value of 80.0 μM against the normal cell lines exhibiting exceptionally high selectivity indexes (SI) of 17.4 and 16. 5 against the examined cell lines, respectively. **T-1-MBHEPA** increased the percentage of apoptotic MCF7 cells in early and late stages, respectively, from 0.71 % to 7.22 % and from 0.13 % to 2.72 %, while the necrosis percentage was increased to 11.41 %, in comparison to 2.22 % in control cells. Furthermore, **T-1-MBHEPA** reduced the production of pro-inflammatory cytokines TNF-α and IL-2 in the treated MCF7 cells by 33 % and 58 %, respectively indicating an additional anti-angiogenic mechanism. Also, **T-1-MBHEPA** decreased significantly the potentialities of MCF7 cells to heal and migrate from 65.9 % to 7.4 %. Finally, **T-1-MBHEPA**'s oral treatment didn't show toxicity on the liver function (ALT and AST) and the kidney function (creatinine and urea) levels of mice.

Peer review under responsibility of King Saud University.

* Corresponding authors at: Department of Pharmaceutical Sciences, College of Pharmacy, AlMaarefa University, Riyadh 13713, Saudi Arabia(E.B. Elkaeed), Pharmacognosy and Medicinal Plants Department, Faculty of Pharmacy (Boys), Al-Azhar University, Cairo 11884, Egypt(A.M. Metwaly).

E-mail addresses: ibrahimeissa@azhar.edu.eg (I.H. Eissa), redayousof@azhar.edu.eg (R.G. Yousef), Hazemelkady@azhar.edu.eg (H. Elkady), mohamedelkady1565.el@azhar.edu.eg (M.A. Elkady), ekaeed@um.edu.sa (E.B. Elkaeed), ametwaly@azhar.edu.eg, ametwaly@azhar.edu.eg (A.M. Metwaly).

https://doi.org/10.1016/j.jsps.2023.101852
Received 12 August 2023; Accepted 30 October 2023
Available online 2 November 2023

1. Introduction

According to the WHO, cancer is of the top causes of mortality and disability, accounting for almost 10 million deaths in 2020, or around one in every six deaths (Elkady et al., 2022). With environmental changes and degradation, cancer has steadily become a huge danger that affects human health globally (Thakur and Pathania 2020, Ali et al., 2021). Fighting cancer was found to be possible through anti-angiogenesis mechanisms, as malignant cells are usually associated with increased vascularity (Fathi Maroufi et al., 2020, Lugano et al., 2020). Also, growth factors and their receptors can play a role in tumor development; a main example of this is the VEGFR-2 which has been linked to cell proliferation, differentiation, and survival in many types of cancers (Wang et al., 2020). Interestingly, literature has provided us with the ability to target VEGFR-2 receptors as an anticancer strategy due to their overexpression in cancerous cells (Yan et al., 2015, Bai et al., 2020). Additionally, recent studies have noticed a link between VEGFR-2 over-expression and greater resistance to cancer medications, increased angiogenesis (Shah et al., 2021) and reduced apoptosis (Spannuth et al., 2009).

However, VEGFR-2 inhibitors, were associated with serious side effects include hypertension (Li et al., 2018), proteinuria (Tesařová and Tesař 2013), bleeding events (Fontanella et al., 2014), germline polymorphisms (Erdem et al., 2012)and reversible posterior leukoencephalopathy syndrome (Levy et al., 2014, Li et al., 2018). Additionally, some individuals may experience gastrointestinal disturbances such as nausea, diarrhea, or constipation. Fatigue and weakness have also been reported as potential side effects. In rare cases, more serious adverse events like cardiac toxicity or thromboembolic events may occur, warranting careful monitoring and management during treatment (Hartmann et al., 2009, Huillard et al., 2014, Fujita et al., 2017). These side effects highlight the urgency for new drug research. Safer alternatives are essential. Advancing novel VEGFR-2 inhibitors can improve treatment efficacy and patient well-being, ultimately enhancing cancer care.

Computer-assisted drug discovery (CADD) approaches were employed to enhance the drug-likeness, pharmacokinetics, and pharmacodynamics of novel drug candidates (Reker and Schneider 2015, Yang et al., 2019). These techniques encompass various approaches, such as molecular design (Elton et al., 2019), docking simulations (Fan et al., 2019), ADMET (Absorption, Distribution, Metabolism, Excretion, and Toxicity) (Ferreira and Andricopulo 2019) prediction, and DFT (Density Functional Theory) (Obot et al., 2015). These computational tools are employed with the objective of identifying compounds that exhibit promising anticancer activity in several researches (Nascimento et al., 2022, NDC and Campos 2022, del Carmen Quintal Bojórquez and Campos 2023, Elkady et al., 2023).

Our laboratory has employed the CADD techniques to design and synthesize new inhibitors for VEGFR-2. These inhibitors encompass diverse classes and derivatives, including quinolones (Taghour et al., 2022), isatins (Elkaeed et al., 2022), nicotinamides (Elkaeed et al., 2022, Yousef et al., 2022), thiazolidines (Taghour et al., 2022, Taghour et al., 2022), pyridines (Yousef et al., 2022), naphthalenes (Elkaeed et al., 2022), and indoles (Elkaeed et al., 2022). This manuscript introduces **T-1-MBHEPA**, a novel lead anti-VEGFR-2 compound, that was synthesized for the first time and shown promising *in silico* and *in vitro* anticancer properties.

1.1. Rational

The ATP binding pocket of VEGFR-2 comprises four distinct regions that are crucial for effective ligand binding (Huang et al., 2012). The first region, known as the adenine binding region or hinge region, is characterized by two critical amino acids, Cys917 and Glu915, that enable efficient binding with a specific ligand (Luo et al., 2017). The second region, the gatekeeper region, acts as a spacer between the hinge region and the DFG motif region and is a hydrophobic pocket that is crucial for achieving optimal ligand binding (Machado et al., 2015). The third region, the DFG motif region, is made up of Asp1044 and Glu883 residues and is essential for hydrogen bonding interactions, which contribute to the formation of a tight binding complex (Wang et al., 2013). Finally, the allosteric pocket, a hydrophobic pocket, is necessary for tight hydrophobic interactions and requires a hydrophobic tail for optimal ligand binding (Dietrich et al., 2010).

To achieve ideal fitting in the ATP binding site of VEGFR-2, VEGFR-2 inhibitors must possess four key pharmacophoric features (Fig. 1**.a**). The first feature is a heteroaromatic structure that contains at least one hydrogen bond acceptor to form hydrogen bonding with Cys917 and Glu915 in the hinge region. The second feature is a spacer moiety, typically phenyl derivatives that can form hydrophobic interactions in the gatekeeper region. The third feature is a pharmacophore moiety consisting of at least one hydrogen bond acceptor and one hydrogen bond donor to form hydrogen bonding interactions with Asp1044 and Glu883 in the DFG motif region. Finally, a hydrophobic tail is required to occupy the allosteric hydrophobic pocket of VEGFR-2 and form tight hydrophobic interactions (Shi et al., 2016, Elwan et al., 2022).

As part of our ongoing efforts, we have developed a new semi-synthetic compound (**T-1-MBHEPA**) with specific structural features that enable it to interact optimally with the various regions of the VEGFR-2 ATP binding pocket. **T-1-MBHEPA** contains a xanthine moiety as a heteroaromatic structure that is intended to occupy the hinge region of the ATP binding pocket. To target the gatekeeper region, we incorporated an *N*-phenylacetamide moiety. Additionally, a formyl hydrazone group was also utilized to facilitate hydrogen bonding interactions with Asp1044 and Glu883 in the DFG motif region. Finally, we have included a 3-methylphenyl moiety as a hydrophobic tail to target the allosteric pocket. These structural features of **T-1-MBHEPA** (Fig. 1**.b**) have been carefully selected based on our understanding of the pharmacophoric requirements of VEGFR-2 inhibitors, and we anticipate that **T-1-MBHEPA** will exhibit improved binding affinity and selectivity towards VEGFR-2.

Introducing **T-1-MBHEPA** as a novel semisynthetic VEGFR-2 inhibitor derived from the well-established safe compound, theobromine in addition to the safety assessments that will be conducted through *in silico*, *in vitro*, and *in vivo* studies to ensure its suitability for further development and potential clinical use. This innovative approach holds promise in advancing targeted therapies with improved safety profiles for cancer treatment.

2. Materials and methods

2.1. Docking studies

The evaluation of **T-1-MBHEPA** against VEGFR-2 was conducted using the MOE 2019 software (Elkady et al., 2023). A detailed and comprehensive explanation of the findings can be found in the **supplementary section**.

2.2. MD simulations studies

The stability of the VEGFR-2_**T-1-MBHEPA** complex, the strength of interactions, and the differences between the apo and holo structures were evaluated by running a 100-ns classical unbiased MD simulation in GROMACS 2021. The CHARMM-GUI web server's solution builder module was used to prepare the input files (Elkaeed et al., 2022, Elkaeed et al., 2022). An elaborate clarification is included in the **supplementary section**.

2.3. Binding free energy calculation using MM-GBSA

With the use of the gmx_MMPBSA program, we were able to evaluate the binding strength using the Molecular Mechanics Generalized Born Surface Area (MM-GBSA) approach (Elkaeed et al., 2022). An elaborate

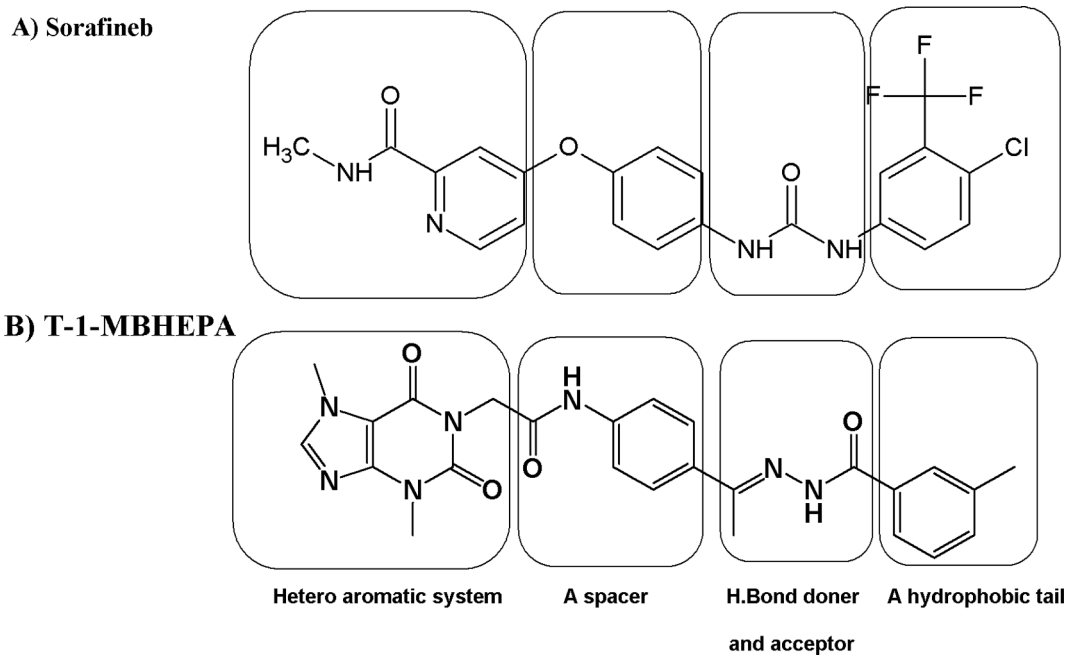

Fig. 1. The pharmacophoric requirements of VEGFR-2 inhibitors in A) Sorafenib and B) **T-1-MBHEPA.**

clarification is included in the **supplementary section**.

2.4. ED Analysis

PCA of the mass-weighted covariance matrix (C) of a selected group of atoms reveals correlated mobility along MD trajectories. In this case, PCA was used to observe the movement of alpha carbons in amino acids (Glu826:Leu1161) (Amadei et al., 1993).

2.5. Bidimensional projections analysis

To make a direct comparison between the frames in the reduced subspace, we first merged the apo-protein and complex trajectories, then aligned them to the apo-protein configuration we obtained after equilibration, then constructed a new C matrix for the combined trajectories, and finally projected each trajectory onto the new C matrix. As a means of gauging the degree to which the two trajectories are similar, we plotted the projection on the first three eigenvectors by using different pair combinations of eigenvectors (Papaleo et al., 2009).

2.6. DFT

Was achieved for **T-1-MBHEPA** by Gaussian 09 and GaussSum3.0 programs. An elaborate clarification is included in the **supplementary section**.

2.7. ADMET and toxicity studies

ADMET studies were achieved for **T-1-MBHEPA** by Discovery Studio 4.0 (Taghour et al., 2022). An elaborate clarification is included in the **supplementary section**.

2.8. Semi-synthesis of T-1-MBHEPA

2.8.1. Synthesis of N-(4-acetylphenyl)-2-chloroacetamide (the key intermediate 4)

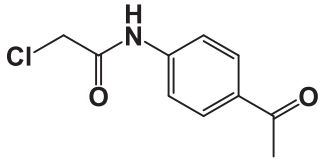

A mixture of *p*- aminoacetophenone **3** (0.8 g, 0.005 mol) and chloroacetylchloride (0.6 g, 0.4 mL, 0.005 mol) in DMF (10 mL) was stirred for 8 h in an ice salt bath in the presence of $NaHCO_3$ (0.9 g, 0.011 mol). After being acidified with HCl, the reaction mixture was poured onto water. The obtained precipitate was filtered, dried, and crystallized from methanol.

White powder (yield, 80 %); ^{1}H NMR (500 MHz, DMSO-d_6) δ 10.63 (s, 1H), 7.92 (d, J = 8.8 Hz, 2H), 7.70 (d, J = 8.7 Hz, 2H), 4.28 (s, 2H), 2.50 (s, 3H); ^{13}C NMR (126 MHz, DMSO-d_6) δ 197.04, 165.74, 143.33, 132.78, 130.03, 119.21, 44.13, 26.95 for $C_{10}H_{10}ClNO_2$ (211.65).

2.8.2. Synthesis of N-(4-acetylphenyl)-2-(3,7-dimethyl-2,6-dioxo-2,3,6,7-tetrahydro-1H-purin-1-yl)acetamide (the key intermediate 5)

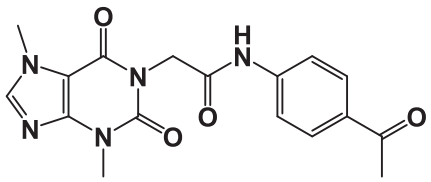

A mixture of potassium 3,7-dimethyl-3,7-dihydro-1*H*-purine-2,6-dione **2** (0.5 g, 0.002 mol) and *N*-(4-acetylphenyl)-2-chloroacetamide **4** (0.4 g, 0.002 mol) in DMF (10 mL) was heated on a water bath for 8 h in the presence of catalytic amount of potassium iodide. The reaction mixture was then poured on crushed ice and the produced precipitate was filtered, dried, and crystallized from ethanol.

White powder (yield, 72 %); ^{1}H NMR (500 MHz, DMSO-d_6) δ 10.58 (s, 1H), 8.04 (s, 1H), 7.94 – 7.85 (m, 2H), 7.71 – 7.61 (m, 2H), 4.68 (s, 2H), 3.85 (s, 3H), 3.40 (s, 3H), 2.49 (s, 3H); ^{13}C NMR (126 MHz, DMSO-d_6) δ 196.96, 166.92, 154.62, 151.37, 149.01, 143.74, 143.56,

132.37, 129.99, 118.84, 107.06, 44.08, 33.68, 29.93, 26.86 for $C_{17}H_{17}N_5O_4$ (355.35).

2.8.3. Synthesis of 2-(3,7-dimethyl-2,6-dioxo-2,3,6,7-tetrahydro-1H-purin-1-yl)-N-(4-(1-(2-(3-methylbenzoyl)hydrazono)ethyl)phenyl) acetamide (T-1-MBHEPA)

N-(4-Acetylphenyl)-2-(3,7-dimethyl-2,6-dioxo-2,3,6,7-tetrahydro-1*H*-purin-1-yl)acetamide **5** and 3-methylbenzohydrazide **8** were mixed and thoroughly dissolved in a round bottom flask containing absolute ethanol (25 mL). Next, the entire mixture was refluxed for 6 h while being catalysed by 3 drops of glacial acetic acid. The mixture was concentrated and cooled following the reaction. The obtained product was filtered and purified *via* crystallisation from methanol.

White crystal (yield, 75 %); m. p. = 215–217 °C; IR (KBr) ν cm^{-1}: 3292 (NH), 1707, 1670 (C = O); ^{1}H NMR (400 MHz, DMSO-d_6) δ 10.66 (s, 1H), 10.42 (s, 1H), 8.08 (s, 1H), 7.83 (m, 2H), 7.70 (m, 2H), 7.63 (m, 2H), 7.33 (d, J = 4.4 Hz, 2H), 4.70 (s, 2H), 3.91 (s, 3H), 3.45 (s, 3H), 2.40 (s, 3H) 2.33 (s, 3H); ^{13}C NMR (101 MHz, DMSO-d_6) δ 166.59, 166.54, 157.64, 154.66, 151.37, 148.99, 143.76, 140.54, 135.44, 131.44, 128.84, 125.49, 127.71, 127.44, 119.05, 107.07, 43.92, 33.67, 29.93, 21.41, 15.88. Mass (*m/z*): 487 (M^+, 45 %), and 278 (100 %, base peak); Anal. Calcd. For $C_{25}H_{25}N_7O_4$ (487.52): C, 61.59; H, 5.17; N, 20.11; Found: C, 61.78; H, 5.40; N, 20.32 %.

2.9. In vitro VEGFR-2 inhibition

Was achieved for **T-1-MBHEPA** by Human VEGFR-2 ELISA kit. An elaborate clarification is included in the **supplementary section**.

2.10. In vitro EGFR and PDGFRβ inhibitory assays

Was achieved for **T-1-MBHEPA** by Human **EGFR and PDGFRβ** ELISA kit. An elaborate clarification is included in the **supplementary section**.

2.11. In vitro antiproliferative and safety activities

The MTT procedure was employed to assess the *in vitro* antiproliferative and safety activities of **T-1-MBHEPA** against HepG2, MCF7, and Vero cell lines (Alley et al., 1988, Van de Loosdrecht et al., 1994). These methods, along with a detailed explanation, can be found in the **supplementary section**.

2.12. Apoptosis analysis

Apoptosis in MCF7 cell lines induced by **T-1-MBHEPA** was assessed using flow cytometry analysis. A comprehensive explanation of this technique and its methodology can be found in the **supplementary section**.

2.13. Inhibition of inflammatory mediators assay

T-1-MBHEPA's effects on IL-2 and TNF in MCF7 cell lines were evaluated using qRT-PCR, utilizing the Qiagen RNA extraction kit and the BioRad syber green PCR master mix. An elaborate clarification is included in the **supplementary section**.

2.14. Scratch assay

The assessment of **T-1-MBHEPA** against MCF7 cell lines was carried out to investigate its potential to promote cell healing and migration post-treatment. A detailed and thorough explanation of the experimental design and methodology can be found in the **supplementary section**.

2.15. In vivo assay of liver and renal function test in mice

The *in vivo* assays followed a research protocol that received authorization from the Research Ethics Committee for clinical studies at the Faculty of Pharmacy, Al-Azhar University in Cairo, Egypt. The studies were carried out at the same institution. The research protocol was assigned the approval number Azhar-Pharmacy-2023–011.

2.15.1. Determination of LD_{50}

The lethal dosage (LD_{50}) evaluation is utilized as a key criterion, for evaluating acute toxicity and as the first step in the process of screening of the testing chemicals for potential toxicity (Chinedu et al., 2013). Thus, the goal of the current investigation was to determine the mice LD_{50} of T-1-MBHEPA, to clarify the dose range to be chosen for a follow-up investigation. Thirty BALB/c male mice were used, given 1, 3 and 5 gm/kg single dose orally (3 equal-sized groups, n = 10), and the animals were monitored for 24 h to check for any deaths. The LD_{50} was only noticed at 5 gm/kg, the other doses were well tolerated.

2.15.2. Experimental design for assessing the liver and renal functions in mice

A total of 18 adult male BALB/c mice of 17–20 gm body weight were used for the two independently dose experiments 100 mg and 200 mg/kg oral single dose. Both experiments are allocated randomly to three equal-sized treated groups (n = 6). The regimens were assigned as follows:

Group I: Six mice were provided with standard diet pellets and drinking tap water ad libitum during the experiment, these animals served as normal control group.

Group II: Six mice were orally administered with (100 mg/kg) single dose, these animals served as 100 mg treated group.

Group III: Six mice were orally administered with (200 mg/kg) single dose, these animals served as 200 mg treated group.

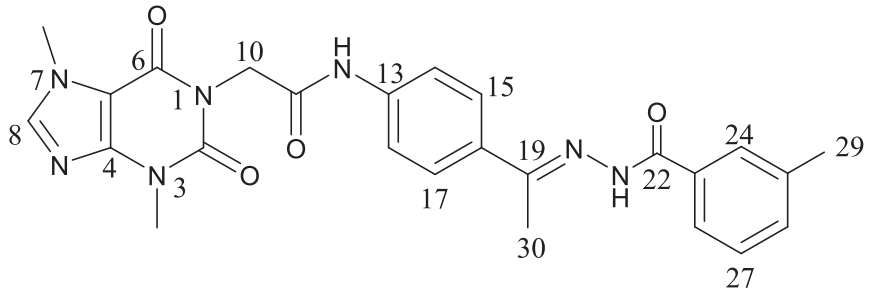

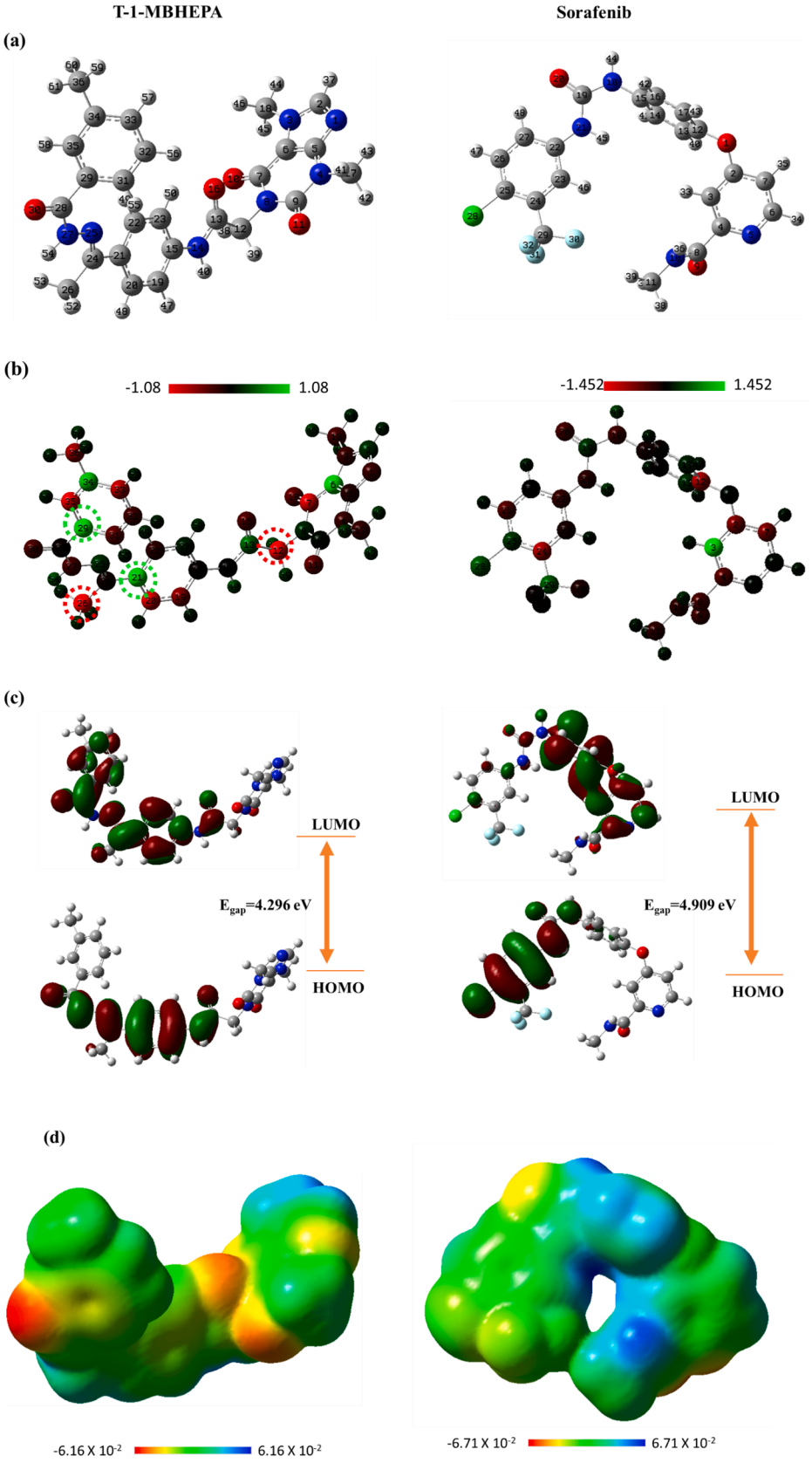

Fig. 2. The optimized geometry (a), the Mullikan atomic charge distribution (b), the frontier molecular orbitals (c), the electrostatic potential (d), the total density of states (e), and the QTAIM maps (f and g) at B3LYB/6–311++G(d,p) for **T-1-MBHEPA and sorafenib**.

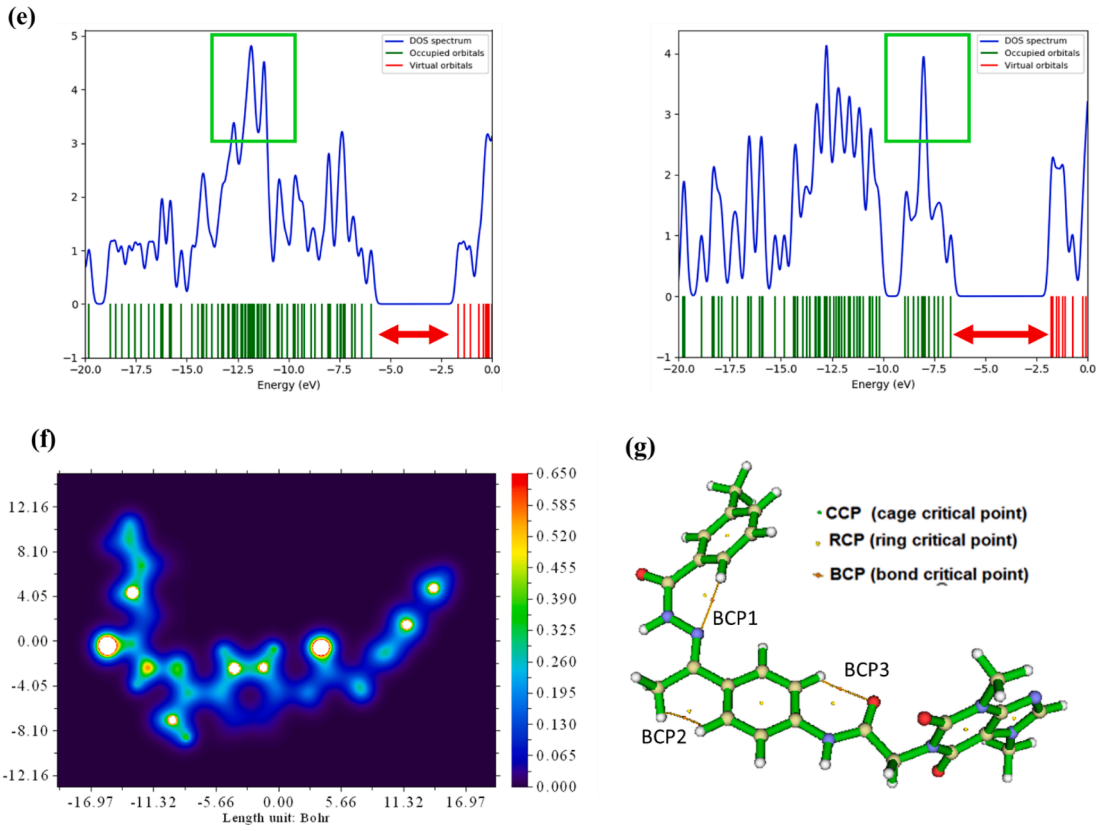

Fig. 2. (*continued*).

3. Results

3.1. DFT studies

Following geometry optimization of the designed compound **T-1-MBHEPA** and the reference compound sorafenib at the DFT/B3LYP/6–311++G (d, p) theory level, a Mulliken analysis was performed to examine the charge distribution function. The figures from Fig. 2**.a** to Fig. 2**.e** represent a comparison between the two compounds and the calculated total ground energy, dipole moment, ionization potential and the electron affinity of the two compounds are listed in Table 1. The labeled optimized molecular schemes are presented in Fig. 2**.a** while Fig. 2**.b** shows the results of the Mulliken population study which was utilized to ascertain the atomic charge values. Interstingly, **T-1-MBHEPA** exhibits considerable charge delocalization, although the dipole moment values of **T-1-MBHEPA** and sorafenib are relatively close. The most positively charged carbon atoms in the **T-1-MBHEPA** molecule are C19 and C21, which are available for assault by nucleophilic targets. Positive charges are concentrated over the hydrogen atoms. Additionally, the most negative carbons in the **T-1-MBHEPA** are C12 and C26. All oxygen and nitrogen atoms, except for N8 and N25, are negative.

The frontier molecular orbital analysis has been investigated to provide additional insight into the reactivity of **T-1-MBHEPA** compared to sorafenib. The energy gaps of the examined compounds were computed using the HOMO and LUMO orbital energies, and it was shown that sorafinib had a greater E_{gap} than T-1-MBHEPA, Fig. 2**.c.** In general, molecules having a wider energy gap are more kinetically stable and less chemically reactive. Hence, **T-1-MBHEPA** can quickly transfer electrons to acceptor. Such results support that **T-1-MBHEPA** is biologically reactive.

For a deeper understanding of **T-1-MBHEPA**'s chemical reactivity, computational indices that depend on HOMO and LUMO energies, such as chemical potential (μ), global softness (σ), global hardness (η), electron affinity (EA), and electrophilicity index (ω), are computed and are compared to those of sorafenib. Our DFT results in Table 1 showed that **T-1-MBHEPA** is more softer and more active than sorafenib (Wang and Husein 2023).

To understand how the electronic charge is dispersed inside **T-1-MBHEPA** and to forecast how it would bond to its target, estimates of the molecular electrostatic potential have been made. Fig. 2**.d** shows the 3D potential surface maps. It is seen that the negative potential regions (red) are concentrated over oxygen atoms and are open to electrophilic assaults. A positive potential surface that is concentrated over hydrogen atoms (blue regions) will be the target of nucleophilic assaults. The green zones over the resonance system are prepared for hydrophobic interactions.

Furthermore, the total density of states (TDOS) analysis has been done, and **Figure S1** shows the spectra of both **T-1-MBHEPA** and sorafenib. For easier visual comparison, the red arrows in **Figure S1** show the band gaps of each molecule.

The Quantum theory of atoms in molecules (QTAIM) has been

Table 1
The DFT calculated global reactivity parameters for **T-1-MBHEPA**.

	IP	EA	μ (eV)	χ (eV)	η (eV)	σ (eV)	ω (eV)	Dm (Debye)	TE (eV)	ΔN_{max}	ΔE (eV)
T-1-MBHEPA	5.944	−1.648	−2.148	2.148	3.796	0.263	8.755	6.614	−39521.4	0.566	−8.755
Sorafebib	6.683	1.773	−4.228	4.228	2.455	0.407	21.939	6.970	−54824.7	1.722	−21.939

studied for **T-1-MBHEPA** using topological analysis utilizing the Multiwfn program based on bond bathes, bond critical points (BCP), and QTAIM parameters. The QTAIM parameters electron density (ρ), Laplacian ($\nabla^2\rho$), and energy density H(r) were also calculated for **T-1-MBHEPA** using the AIMALL software. The estimated values are shown in **Table S1**, and **Figures S2 and S3** show the molecular graph and the main generated QTAIM bonding bath with relative critical points.

Moreover, **Figure S4.** depicts the detailed bond critical points (BCP). **T-1-MBHEPA** is stable thanks to internal noncovalent bonding, which gives the molecule its stability, according to the computed (ρ), ($\nabla 2\rho$), and H(r).

3.2. Molecular docking

In the current investigation, sorafenib was fixed as a reference VEGFR-2 inhibitor. Sorafenib docked with three H-bonding contacts with Cys919, Glu885, and Asp1046, as seen in Fig. 3. Additionally, it interacted with the hydrophobic pocket made by Leu889, Leu1019, and Ile892 *via* three hydrophobic bonds.

T-1-MBHEPA's affinity for ATP-binding site of VEGFR-2 was investigated. It was discovered that the compound's purine moiety had the capacity to occupy the hinge area and make an H-bond with Cys917. In addition, the central phenyl part formed hydrophobic contacts with Ala864, Val914, Lys866, and Val846 in the linker region. Additionally, Glu883 and Asp1044 in the DFG motif region can generate two H-bonds with the amide group of **T-1-MBHEPA**. In addition, it perfectly fits the hydrophobic region and interacts with its hydrophobic backbone (Ile886 and Leu887) as presented in Fig. 4 **and Figure S5**.

Sorafenib and **T-1-MBHEPA** attach to VEGFR-2 with the same spatial orientation, as stated by the docking results shown in Figs. 5 and 6. More specifically, the purine, phenyl, amide group, and *o*-tolyl moieties of **T-1-MBHEPA** revealed the same orientation as the *N*-methylpicolinamide, phenoxy, urea, and 4-chloro-3-(trifluoromethyl)phenyl) moieties of sorafenib.

3.3. MD simulations

Production run analyses showed that molecule **T-1-MBHEPA** kept a rather consistent shape and a nearly constant distance from the protein's center of mass. The RMSD values for the VEGFR-2 in VEGFR-2_Sorafenib (blue line) and VEGFR-2_**T-1-MBHEPA** (red line) complexes are shown to have equilibrated at roughly 2.1 Å after around 20 ns (Fig. 5**.a**) with the VEGFR-2_**T-1-MBHEPA** showing a spike from 70 ns to 80 ns. The average RMSD for the **T-1-MBHEPA** compound is shown to be around 3.4 Å in Fig. 5**.b** combared to 1.7 for the Sorafenib. Furthermore, Fig. 5**.c and** Fig. 5**.d** show that the radius of gyration and SASA follow the same trend with a rise around the 70 ns to 80 ns for the VEGFR-2_**T-1-MBHEPA**. As can be seen in Fig. 5**.e**, the total number of H-bonds varies slightly, with an average of around 70 bonds for both systems. Altogether, this indicates the stability of the protein structure. The RMSF plot (Fig. 5**.f**) reveals that amino acids are highly stable (have fluctuation values of less than 2 Å), except for the N-terminus for both systems (5.3 Å for VEGFR-2_Sorafenib and 7.6 Å for VEGFR-2_**T-1-MBHEPA**), the Tyr994:Asp996 loop of the VEGFR-2_Sorafenib (3.3 Å), the Gly1046:Leu1065 loop of the VEGFR-2_Sorafenib (7.1 Å), Lys1053:Asp1062 for the VEGFR-2_**T-1-MBHEPA** (4.1 Å), and the C-terminus (5.3 Å for the VEGFR-2_Sorafenib and 4.8 Å for the VEGFR-2_**T-1-MBHEPA**). The steady separation of each of the Sorafenib and **T-1-MBHEPA** center of mass from the protein's center of mass, with an average distance of 7.8 Å for both of them, is a strong indicator of binding stability (Fig. 5**.g**).

3.4. MM_GBSA and ProLIF studies

In Fig. 6, we can see the individual contributions to the binding free energy that were computed using the MM-GBSA method. Overall, the **T-1-MBHEPA** molecule has a binding energy of −41 kcal/mol compared to −45.47 Kcal/Mol for Sorafenib, suggesting a similar strong interaction. Binding stability is influenced by electrostatic interactions (-20 Kcal/Mol for Sorafenib compared to −13.21 Kcal/Mol for **T-1-MBHEPA**), but to a much lesser extent than van der Waals interactions (-52.54 Kcal/Mol for Sorafenib compared to −61.62 Kcal/Mol for **T-1-MBHEPA**). Amino acids within 1 nm of the **T-1-MBHEPA** or Sorafenib molecules had their contributions determined by decomposing the free energy (Fig. 7). For **T-1-MBHEPA**, Leu838 (-1.98 Kcal/Mol), Val846 (-1.54 Kcal/Mol), Leu887 (-1.35 Kcal/Mol), Val897 (-1.32 Kcal/Mol), Val914 (-1.26 Kcal/Mol), Leu1033 (-1.05 Kcal/Mol), Cys1043 (-3.81 Kcal/Mol), Asp1044 (-1.07 Kcal/Mol), Phe1045 (-5.05 Kcal/Mol), and Asp1049 (-1.17 Kcal/Mol) are the amino acids that have a contribution less than −1 Kcal/Mol. Similarly, Leu838 (-1.25 Kcal/Mol), Val846 (-1.22 Kcal/Mol), Leu887 (-1.51 Kcal/Mol), Val914 (-1.15 Kcal/Mol), Phe916 (-1.53 Kcal/Mol), Cys917 (-1.11 Kcal/Mol), Leu1033 (-1.16 Kcal/Mol), Cys1043 (-2.71 Kcal/Mol), Asp1044 (-1.21 Kcal/Mol), and

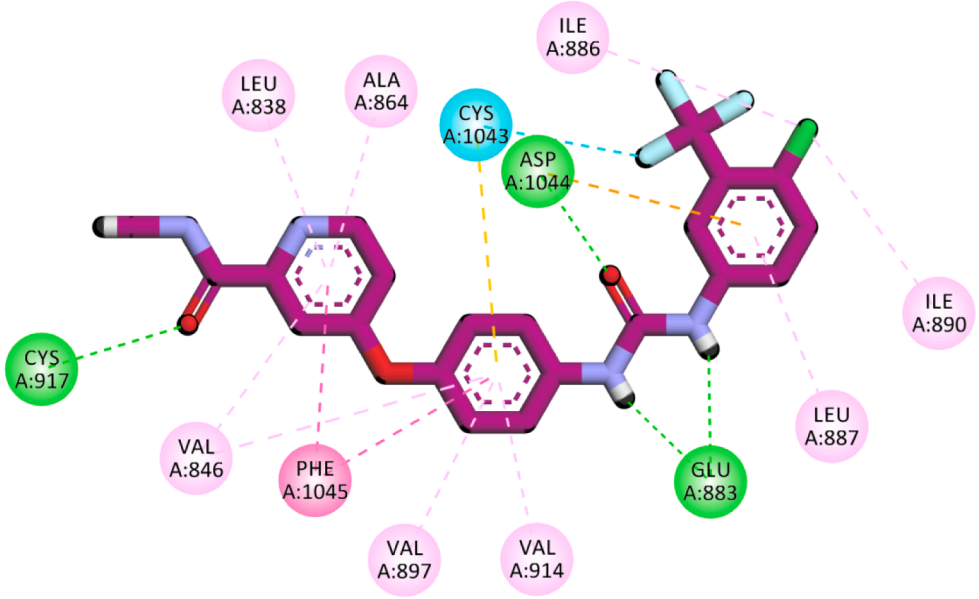

Fig. 3. 2D binding mode of sorafenib inside VEGFR-2.

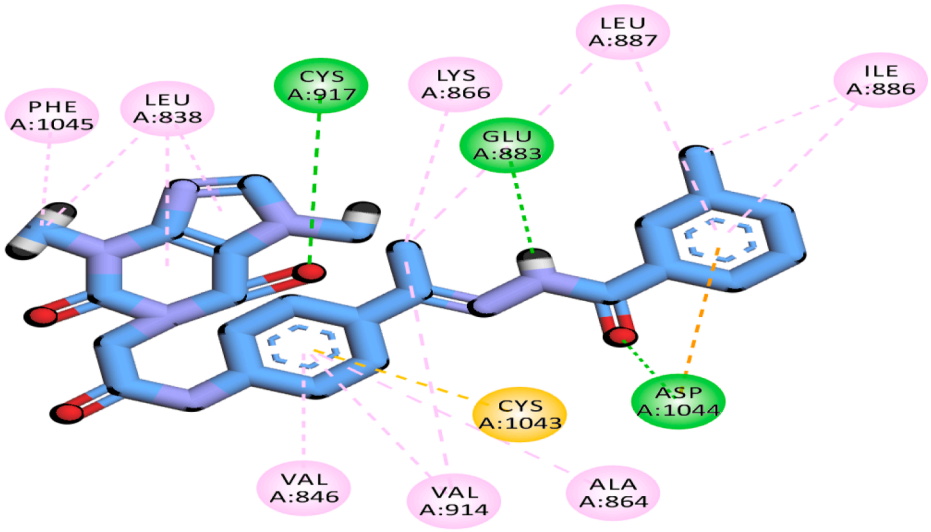

Fig. 4. 2D of **T-1-MBHEPA** inside VEGFR-2 active site.

Phe1045 (-1.43 Kcal/Mol) are the amino acids contributing to the binding of Sorafenib. As can be seen there are seven common amino acids between the two complexes with contribution of less than −1 Kcal/Mol.

Using the ProLIF library we determined that Leu838, Val846, Leu887, Ile890, Val897, Val914, Leu1017, Cys1043, Asp1044, and Phe1045 show very long-lasting hydrophobic contacts with **T-1-MBHEPA** (91.4 percent occurrence or higher) (**Figures S6 A-C**). Additionally, Asp1044 forms H-bonds with an incidence of 84 % while Phe1045 forms Pi-stacking with an incidence of 99 %. In comparison with Sorafenib, we found that Leu838, Val846, Leu887, Ile890, Val897, Val914, Leu1017, Cys1043, Asp1044, and Phe1045 were common amino acids with occurrence of at least 92.7 % for hydrophobic interactions. Additionally, Asp1044 forms a H-bonds with an occurrence of 81 % and Phe1045 forms pi-stacking with occurrence of 83 % (**Figures S7 A-C**). After clustering, representative frames were used in PLIP to extract 3D binding conformations as.pse files (**Figures S8 and S9**). To determine the mode of the binding (DFG-in or DFG-out), we aligned the cluster representatives and observed the orientation of Phe1045. Since it was pointing in the opposite direction of the allosteric site, the binding mode was in the DFG-out (Fig. 8) (Moradi et al., 2023).

3.5. Essential dynamic (ED) studies

The origin of the trajectory's high-amplitude, coordinated motion was located with the use of principal component analysis. The number of eigenvectors that may adequately represent the reduced subspace was calculated by plotting the eigenvalues against the eigenvector index (scree plot). The first eigenvector was responsible for 73.3 % of the total variance by itself, while the first three eigenvectors combined accounted for around 83.1 % of the overall variance (**Figure S10**). Another observation was that the first three eigenvectors have a non-Gaussian distribution, whereas the distribution of the remaining eigenvectors is Gaussian (**Figure S11**).

To quantify the randomness of the motion represented by the first 10 eigenvectors, the cosine content of apo and holo VEGFR-2 simulations was calculated. For both the apo and holo proteins, the cosine content of the first 10 eigenvectors is less than 0.25. (**Figure S12**). Due to this, the top three eigenvectors were chosen to represent the essential subspace. Due to the low degree of overlap (33.1 % according to the RMSIP) between the two subspaces (the first three eigenvectors), it is clear that the two trajectories were sampled differently. RMSIP analysis also found just a 38.2 % similarity between the apo and holo C matrices.

3.6. Bi dimentional projection studies

Projecting each trajectory onto the first three eigenvectors of the combined C matrix yields the findings shown in Fig. 9, where the average structure of the trajectories is represented by a larger marker. In Fig. 9 **A** (projection on the first two eigenvectors), we can see that the two trajectories have distinct average structures and display sampling that only partly coincide. The projection on the first and third eigenvectors, shown in Fig. 9 **B**, reveals that the two average structures are quite similar and have a far higher degree of overlap. Finally, projection on the second and third eigenvectors shows that the two trajectories have little overlap and that there is a large difference between the average structures (Fig. 9**C**). For the first three eigenvectors, porcupine diagrams were used to display the corresponding motion (**Figure S13**). Specifically, the largest motion captured by these three eigenvectors is the Gly1046:Leu1065 loop. The first eigenvector for both trajectories captures the same motion (loop opening), but at different magnitudes. As seen by the second eigenvector, the green apo structure rotates with an opening of the loop, whereas the red holo structure shows a loop - closing. For the third eigenvector, the recorded motion in the apo protein demonstrates the opening of the loop concurrent with the protein becoming more compact; in contrast, the motion caught for the holo protein demonstrates just the protein becoming more compact.

3.7. In silico ADME analysis

ADME properties include the assessment of a number of factors that are crucial not only in assessing the drug's capacity to reach pharmacologically active concentrations at therapeutic goals. Also, ADME may be responsible for adverse impacts caused by accumulation or biotransformation. Hence, ADME assessment can be effective when coupled with *in silico* toxicity models.

In the current study, The ADMET characteristics of **T-1-MBHEPA** were computationally calculated with Discovery Studio®. Compared with sorafenib, the results (**Figure S14**, **Table S2**) show that **T-1-MBHEPA** has an extremely low potential for crossing the blood–brain barrier (BBB). Interstingly, **T-1-MBHEPA** was predicted to be much safer than sorafenib as it was non-hepatotoxic. Both drugs didn't inhibit Cytochrome P450. (CYP2D6). Enthrallingly, **T-1-MBHEPA** has good aqueous solubility and moderate average intestinal absorption, as shown in **Table S2**. Unlike sorafenib, the binding of **T-1-MBHEPA** to plasma proteins was predicted to be less than 90 % implying that a significant portion of **T-1-MBHEPA** will remain unbound and freely available in the bloodstream (Schmidt et al., 2010).

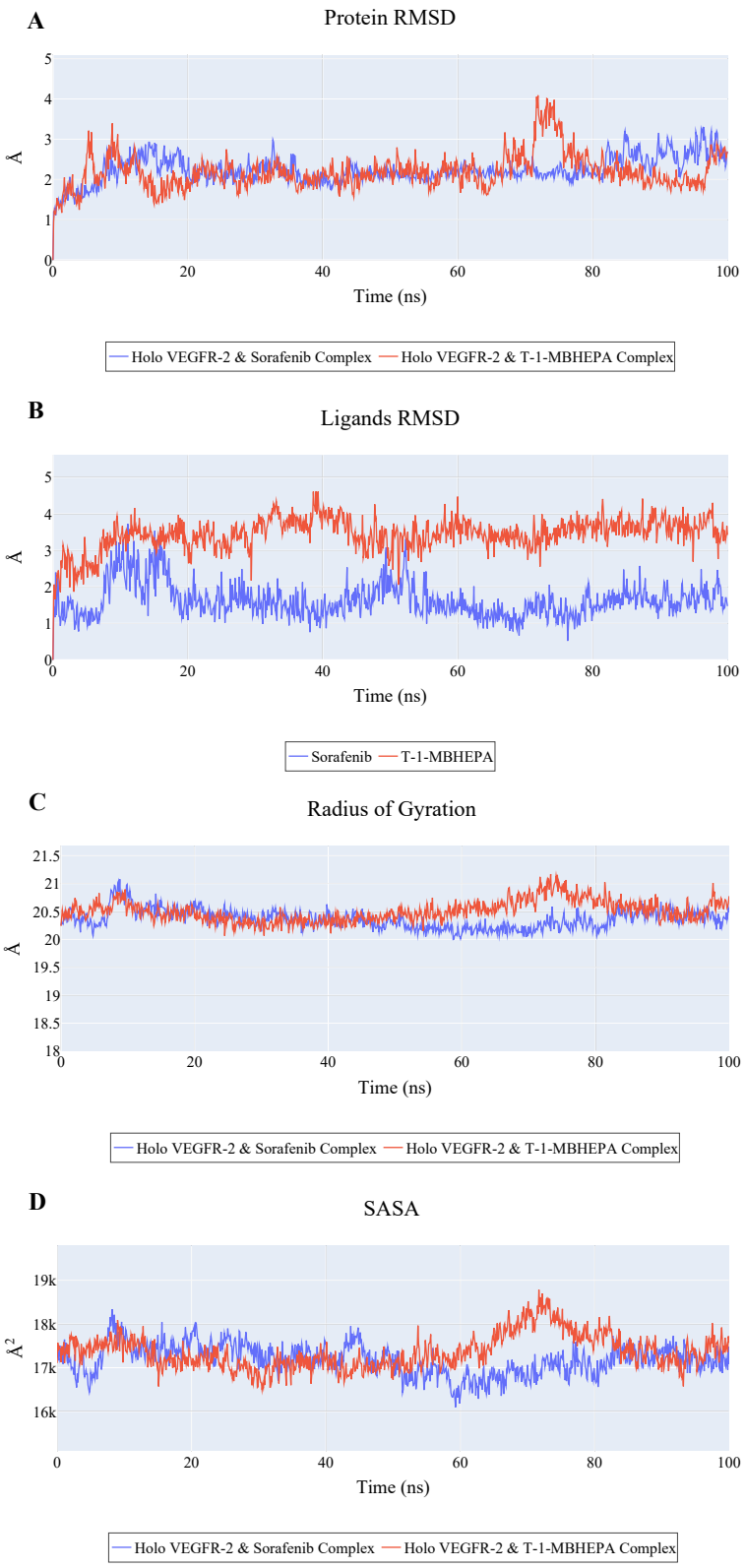

Fig. 5. Shows the **A**) RMSD values from the trajectory for the VEGFR-2 protein in VEGFR-2_Sorafenib (blue line) and VEGFR-2_T-1-MBHEPA complexes (red line), **B**) shows the Sorafenib and **T-1-MBHEPA** RMSD values, **C**) radius of gyration for the VEGFR-2 protein in VEGFR-2_Sorafenib (blue line) and VEGFR-2_T-1-MBHEPA complexes (red line), **D**) SASA for the VEGFR-2 protein in VEGFR-2_Sorafenib (blue line) and VEGFR-2_T-1-MBHEPA complexes (red line), **E**) change in the number of hydrogen bonds for the VEGFR-2 protein in VEGFR-2_Sorafenib (blue line) and VEGFR-2_T-1-MBHEPA complexes (red line), **F**) RMSF for the VEGFR-2 protein in VEGFR-2_Sorafenib (blue line) and VEGFR-2_T-1-MBHEPA complexes (red line), **G**) distance from the center of mass of Sorafenib and **T-1-MBHEPA** from VEGFR-2 protein center of mass. (For interpretation of the references to colour in this figure legend, the reader is referred to the web version of this article.)

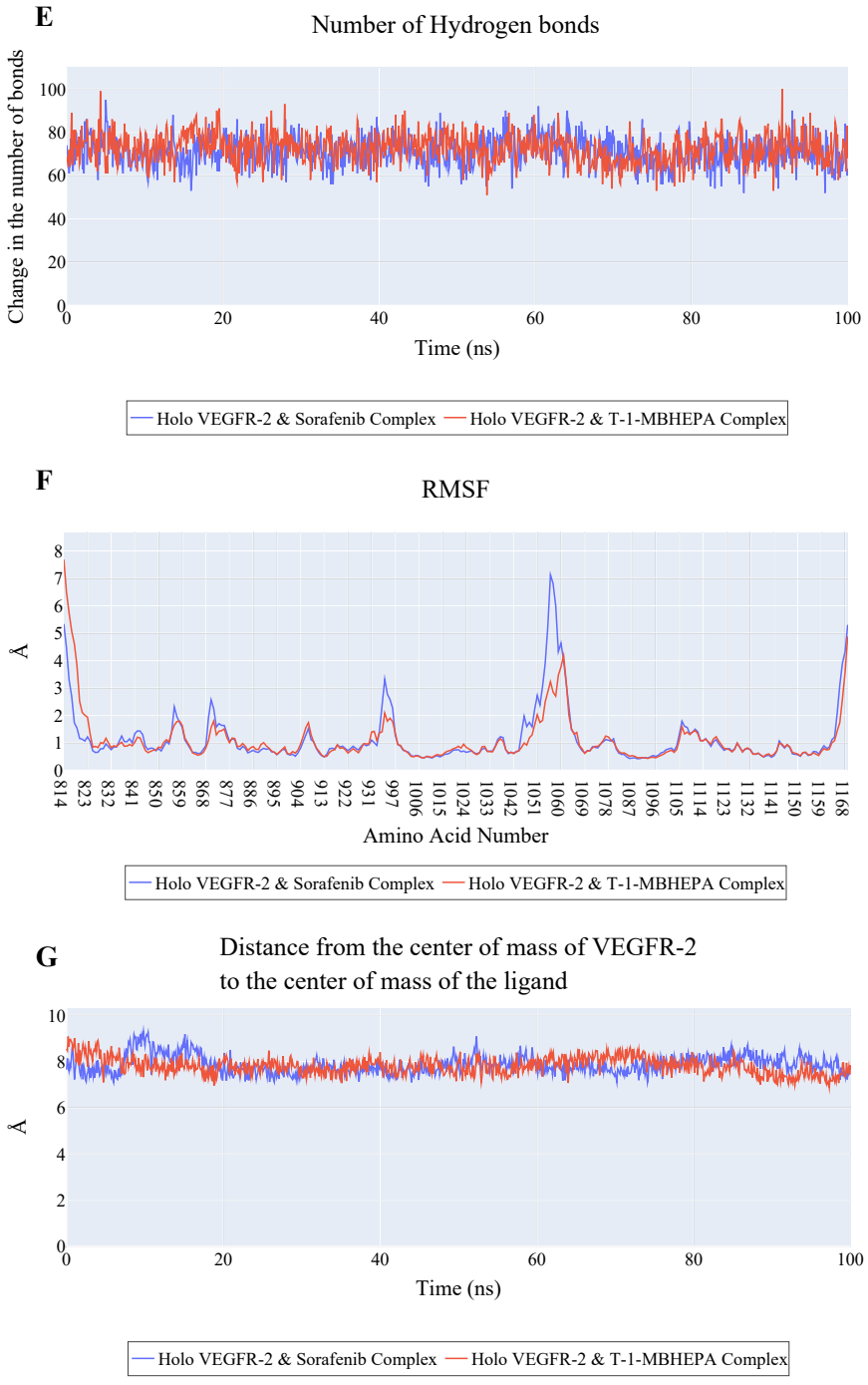

Fig. 5. (*continued*).

3.8. *In silico toxicity studies*

Applying *in silico* methods is crucial when it comes to drug development, as it minimizes the requirement for both *in vitro* and *in vivo* tests. This ultimately leads to reduced delays (Idakwo et al., 2018). Predictive toxicity software based on Structure-Activity Relationship (SAR) can assess a molecule's basic structural descriptors by comparing them with thousands of molecules categorized as toxic or safe (Kruhlak et al., 2012), see the detailed toxicity report in the **Supplementary Data**. Hence, discovery studio software has contributed towards creating eight models for toxicity which include FDA Rodent Carcinogenicity in Rat-female (FDA-C-RF), Ames Mutagenicity (Am M), mouse carcinogenicity (TD_{50}-M), and a rat maximum tolerable dose (MTD-R), oral lethal dose 50 (Oral LD_{50}), Chronic Lowest Observed Adverse Effects Level in rats (C-R-LOAEL) in addition to the dermal (DI) and ocular (OI) irritation potentialities. The designed theobromine derivative **T-1-MBHEPA** showed generally high safety levels in all models as in **Table S3**. Fascinatingly, **T-1-MBHEPA** was anticipated to be much safer than sorafenib in three models (TD_{50}-M, LD_{50}, and C-R-LOAEL). Also, both compounds showed safe patterns in (FDA-C-RF, Am M, DI, and OI). While **T-1-MBHEPA** was predicted to be less safe than sorafenib in MTD-R, the predicted value is very safe.

3.9. *Semi synthesis*

Theobromine **1** was first converted to its potassium salt **2** by

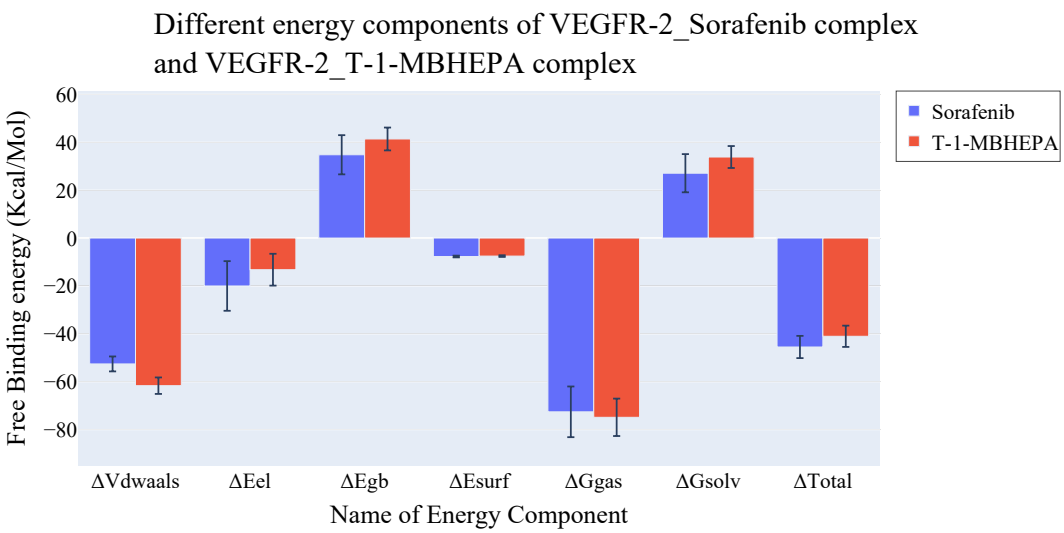

Fig. 6. Energetic components of MM-GBSA. Bars represent the standard deviations.

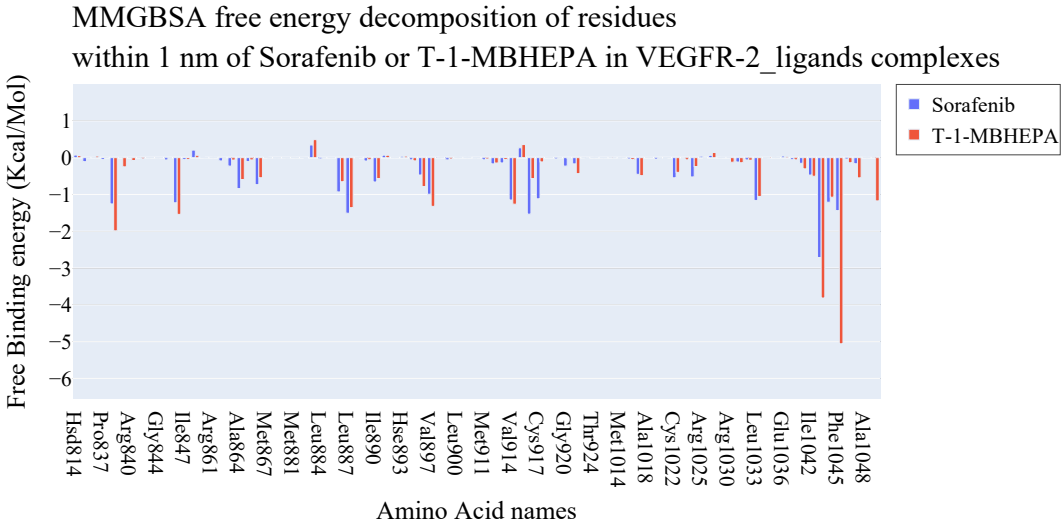

Fig. 7. Binding free energy decomposition of the VEGFR-2_**T-1-MBHEPA** and VEGFR-2_Sorafenib complexes.

refluxing it with alcoholic KOH. *N*-(4-acetylphenyl)-2-chloroacetamide **4** was produced by the reaction of *p*- aminoacetophenone **3** with chloroacetylchloride in DMF using $NaHCO_3$ as a base. Equimolar amounts of **2** reacted with **4** and were refluxed in DMF using potassium iodide as a catalyst to afford the key intermediates compound **5**. Moreover, 3-methylbenzohydrazide **8** was readily prepared by refluxing methyl 3-methylbenzoate **7** with hydrazine hydrate in absolute ethanol. Condensation of compound **5** with benzohydrazide derivative **8** afforded the final target **T-1-MBHEPA** (Scheme 1).

The proton NMR spectrum of **T-1-MBHEPA** (in DMSO-d_6), Fig. 10, displayed two singlet signals for the amidic protons at δH 10.66 and 10.42 ppm, and a singlet signal for the theobromine moiety proton at δH 8.08 ppm. In the aromatic region, eight protons were detected, with six of them overlapping at δH 7.63 ~ 7.83 ppm. The other two protons appeared at δH 7.33 (2H, $J = 4.4$ Hz, H-14 and H-18) suggesting a di-para substitution. On the other hand, the other 2 protons (H-15 and H-17) appeared in the overlapping area. Furthermore, five protons appeared as singlet signals at δH 4.70 ppm corresponding to the methylene group (H-10), two methyl signals of the theobromine unite at δH 3.91 (singlet, H-7) and δH 3.45 (singlet, H-3), and two methyl singlet signals of (H-29 and H-30) which resonated at δH 2.33 and 2.20, respectively. In the ^{13}C NMR spectrum, 25 carbon signals were observed, including four methyls, one methylene, nine sp2 methine, seven quaternary sp2, and four amide carbonyl carbons, which supported the proposed structure's validity.

3.9.1. Biological evaluation

3.9.1.1. In vitro VEGFR-2 inhibition. **T-1-MBHEPA** was specifically designed to be an inhibitor of VEGFR-2, which plays a vital role in regulating angiogenesis (Sivaraj et al., 2013, Modi and Kulkarni 2019). Its promising computational simulations encouraged further investigation into its *in vitro* potential against the VEGFR-2 protein. Interstingly, **T-1-MBHEPA** exhibited significant inhibitory effects on VEGFR-2 protein with an IC_{50} value of 0.121 ± 0.051 μM (**Table S4**), confirming the suppression ability of the compound in both *in silico* and *in vitro*.

3.9.1.2. In vitro EGFR and PDGFRβ inhibitory assays. To ensure the selectivity of **T-1-MBHEPA** towards VEGFR-2, a multikinase inhibitory activity was investigated towards EGFR and PDGFRβ. The findings presented in Table 2 as revealed weak inhibitory activities of **T-1-MBHEPA** against EGFR and PDGFRβ in comparison to the reference

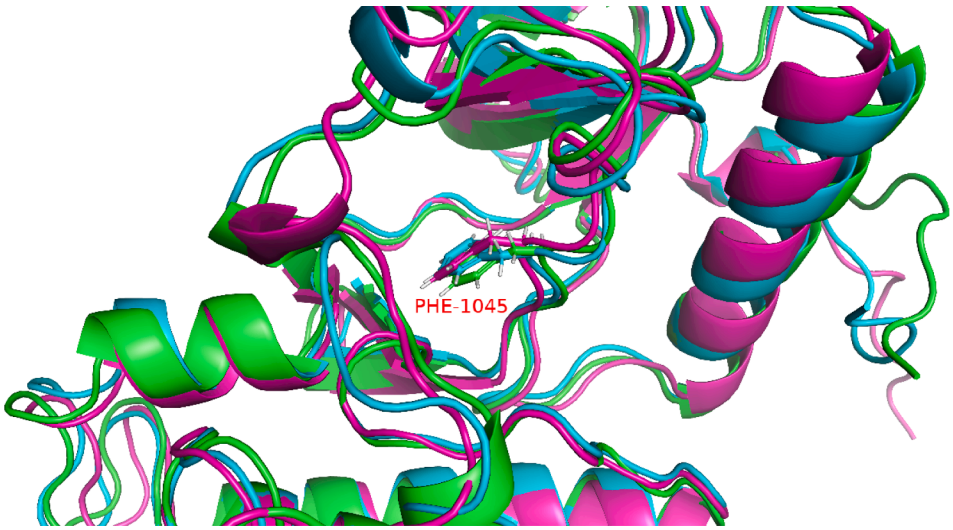

Fig. 8. The orientation of the Phe1045 (of the DFG motif) at the three cluster representatives. As determined from the orientation, the binding is in the DFG-out conformation.

drugs erlotinib and sunitinib. It showed IC_{50} values of 0.355 and 0.179 μM against EGFR and PDGFRβ, respectively. From these results, we can reach two valuable findings. Firstly, **T-1-MBHEPA** has non selectivity against EGFR and PDGFRβ kinases. Secondly, **T-1-MBHEPA** has comparable activities against both EGFR and PDGFRβ with slightly higher activity against PDGFRβ**.** These comparable activities against EGFR and PDGFRβ could be observed in some drugs as foretinib (Kataoka et al., 2012) and pazopanib (Zhu and Rini 2015). Such non-selectivity is due to the high similarity of the active sites of protein kinase family (Kinnings and Jackson 2009).

3.9.2. *In vitro cytotoxicity and safety*

The synthesized compound **T-1-MBHEPA** displayed impressive anti-VEGFR-2 potential both *in silico* and *in vitro*, making it a desirable anticancer agent. *In vitro* tests were conducted to evaluate the cytotoxicity of **T-1-MBHEPA** against breast carcinoma epithelial MCF7 and human liver cancer HepG2 cell lines using sorafenib as a reference drug. Notably, **T-1-MBHEPA** demonstrated effective anticancer properties against these cancer cells with IC_{50} values of 4.85 μM and 4.61 μM, respectively. In comparison, Sorafenib had much lower IC_{50} values of 3.17 μM and 2.24 μM for the same cells tested before (**Table S5**). On the other hand, experiments were carried out on the Vero cell line to confirm the safety and specificity of **T-1-MBHEPA**. The findings showed that **T-1-MBHEPA** revealed a noteworthy IC_{50} value of 80.0 μM and exceptionally high selectivity selectivity indexes (SI) of 16.5 and 17.35 against the two cancer cell lines.

3.9.3. *Apoptosis*

Annexin V and PI double stains were used to study the apoptotic effects of **T-1-MBHEPA** in MCF7 cells (Alanazi et al., 2021). Compared to the control, a concentration of 30.95 μM of **T-1-MBHEPA** increased the percentage of apoptotic MCF7 cells in the early and late stages of apoptosis (respectively, from 0.71 % to 7.22 % and from 0.13 % to 2.72 %), while the necrosis percentage was increased to 11.41 %, in comparison to 2.22 % in control cells (Table 3 & Fig. 11). Therefore, we can conclude that **T-1-MBHEPA** successfully arrested the cell cycle in MCF7 cells and exhibited cytotoxic potentialities that could be related to apoptosis.

3.9.4. *Inhibition of inflammatory mediators*

Chronic inflammation has been recognized as a contributing factor to the development and progression of various types of cancer (Shacter and Weitzman 2002). Inflammatory mediators such as cytokines and chemokines have been shown to play a crucial role in the promotion of cancer cell growth, survival, and metastasis by inducing angiogenesis, suppressing immune surveillance, and causing genetic instability and DNA damage. These molecular processes create a tumor microenvironment that is favorable for cancer cell proliferation and progression, ultimately leading to the development of cancer. Inflammatory mediators have been reported to induce the upregulation of VEGF expression through a multitude of intricate molecular mechanisms involving a variety of intracellular signaling pathways exhibiting synergistic actions to potentiate VEGF expression and consequently enhance its pro-angiogenic functions (Angelo and Kurzrock 2007). Complementary, several studies have shown that VEGFR-2 inhibitors can reduce the production of pro-inflammatory cytokines in various cell types such as interleukins (ILs) (Ou et al., 2009, Tian et al., 2011) and tumor necrosis factor-α (TNF-α) (Zhang et al., 2019).

Accordingly, the levels of TNF-α and IL-2 have been estimated in both treated and control cancer cells. Interestingly, as shown in **Table S6**, **T-1-MBHEPA** reduced the production of pro-inflammatory cytokines TNF-α and IL-2 by 33 % and 58 %, respectively indicating an additional anti-angiogenic mechanism.

3.9.5. *The effect of T-1-MBHEPAon MCF7's migration and healing*

To assess the impact of **T-1-MBHEPA** on the migration and healing of MCF7 cancer cells, researchers used the wound healing assay, which is a cost-effective and straightforward method for measuring cancer cell migration *in vitro* (Jonkman et al., 2014). This technique involves making a scratch on a cancer cell monolayer, measuring the initial diameter, and monitoring the closure of the scratch at specific time intervals for both treated and untreated cells. The researchers compared images of the scratch areas of treated and untreated cell lines after 0 and 48 h (Rodriguez et al., 2005). The results (shown in Table 4 and Fig. 12) indicated that the scratch of the untreated MCF7 cells closed significantly within 48 h, reducing the width by 65.9 %. On the other hand, the scratch width of MCF7 cells treated with **T-1-MBHEPA** decreased by only 7.4 %, indicating that the treatment significantly inhibited the closure of the scratch.

3.9.6. *Liver and renal function test in mice*

3.9.6.1. Effect of 100 and 200 mg/kg T-1-MBHEPAs oral treatment on the liver function levels of ALT and AST of mice. At the end of experiment, the control group showed normal ALT and AST levels (25.2 ± 1.2 and 29.1 ± 1.1). Furthermore, the change in ALT and AST levels among the two

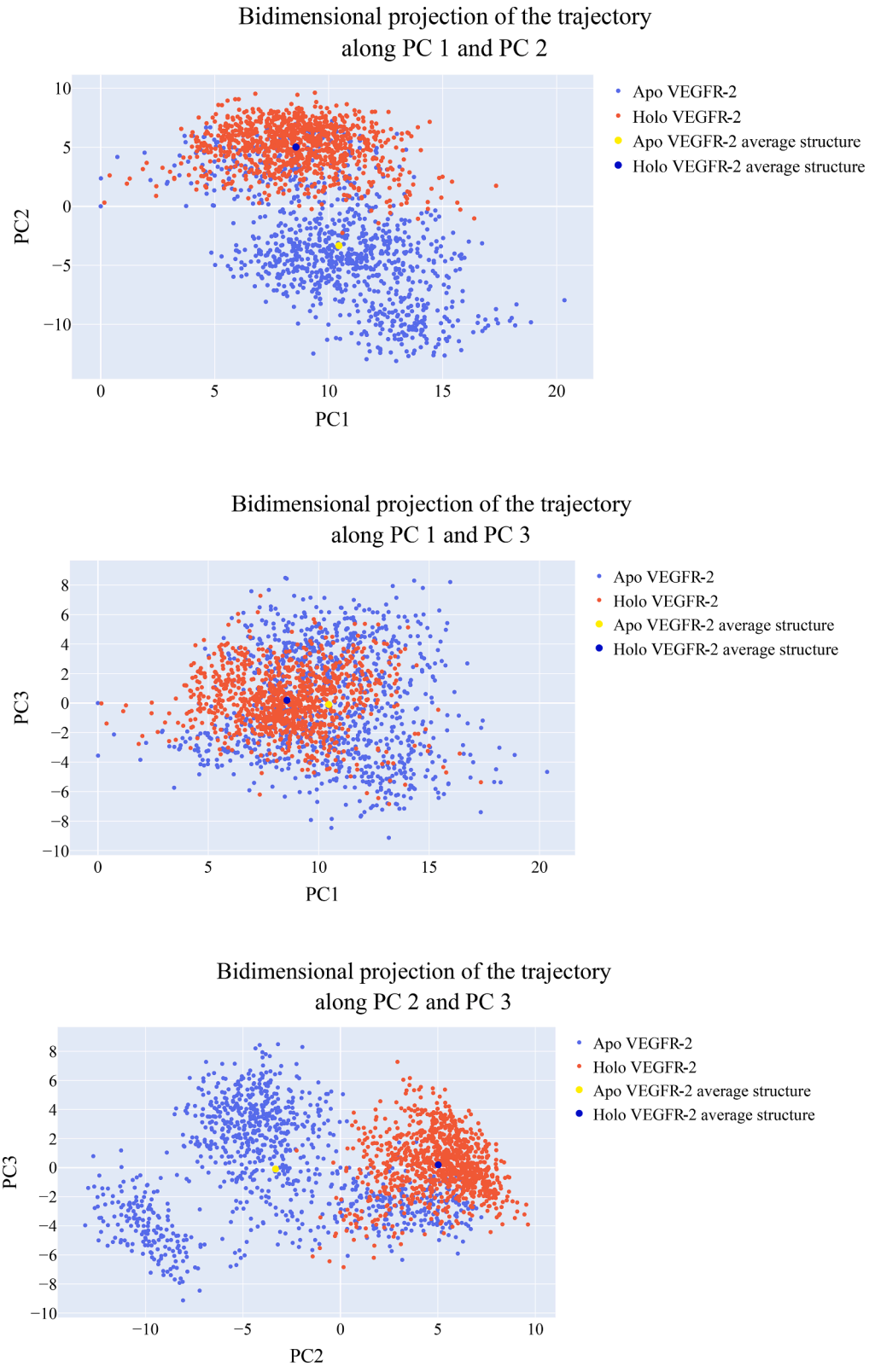

Fig. 9. The projection of each trajectory on A. the first two, B. the first and third and C. the second and third eigenvectors.

independently parallel experiments (group II and group III) showed non-significant changes as the previous manner (25.3 ± 2.1, 29.2 ± 1.1 and 28.9 ± 2.1, 31.7 ± 1.8), respectively, when compared to the control group.

3.9.6.2. Effect of 100 and 200 mg/kg T-1-MBHEPAs oral treatment on the kidney function levels of creatinine and urea of mice. The control group showed normal creatinine and urea levels (0.7 ± 0.02 and 36.9 ± 1.9), respectively. Moreover, the change in creatinine and urea levels among the two independently parallel experiments (group II and group III) showed non-significant changes (0.7 ± 0.03, 0.9 ± 0.02 and 38.9 ± 2.1,

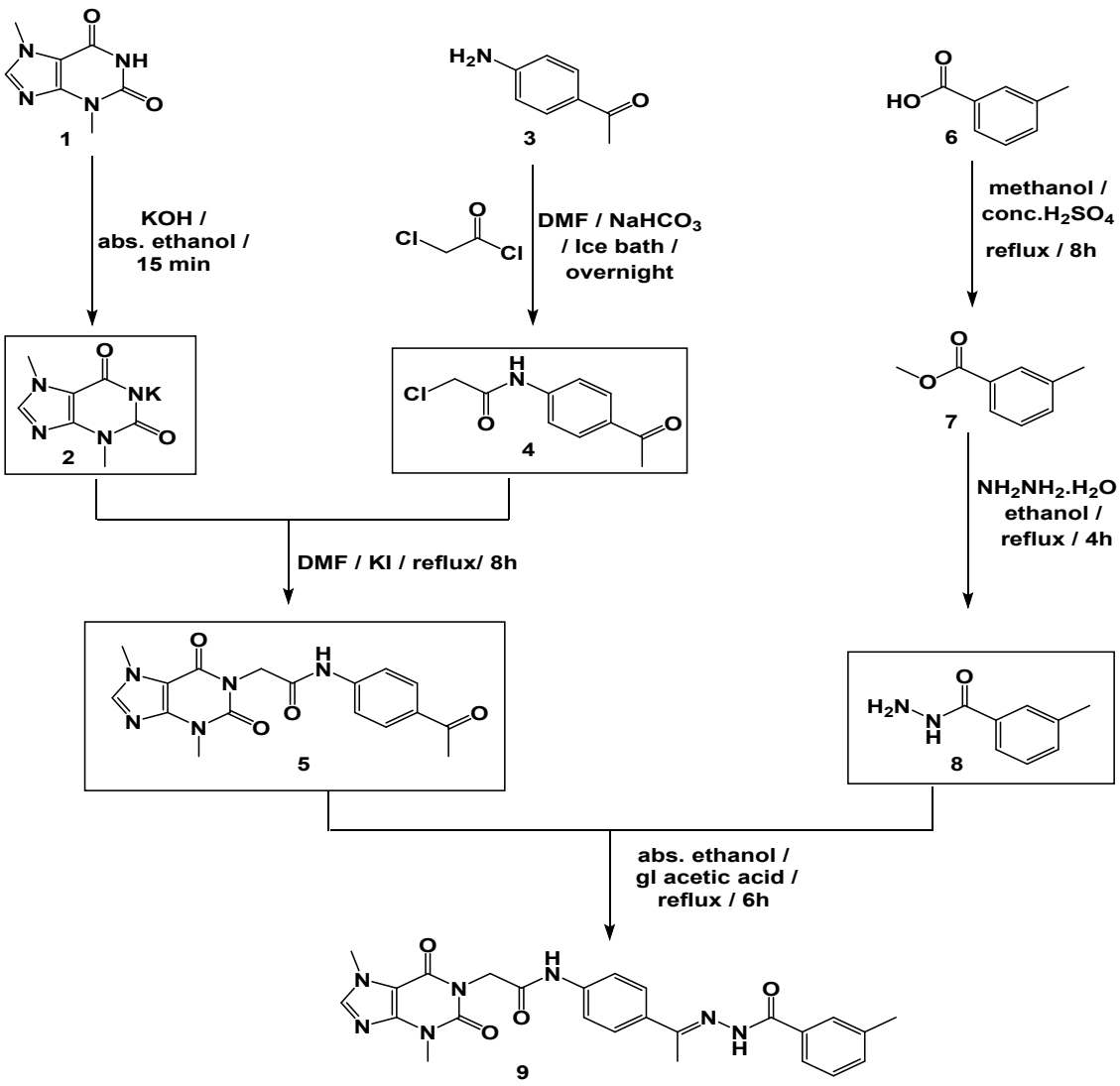

Scheme 1. Semi-synthesis procedure of **T-1-MBHEPA.**

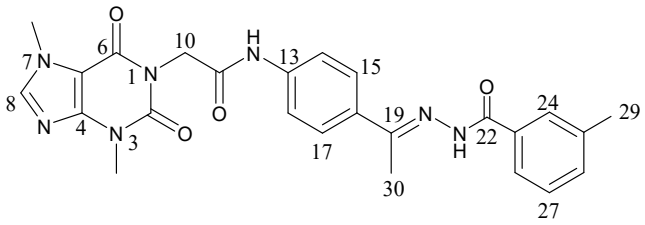

Fig. 10. Chemical structure of **T-1-MBHEP.**

Table 2
Inhibitory activity of **T-1-MBHEPA** against EGFR and PDGFRβ.

Comp.	EGFR (μM/ml)	PDGFRβ (μM/ml)
T-1-MBHEPA	0.355 ± 0.014	0.179 ± 0.009
Erlotenib	0.049 ± 0.002	———
Sunitinib	———	0.085 ± 0.003

43.7 ± 1.8), respectively, when compared to the control group. Also, there was non-significant change in creatinine and urea levels between the two independently parallel experiments (group II and group III) at the end of the experiment.

Table 3
Effect of **T-1-MBHEPA**on stages of the cell death process in MCF7 cells.

Comp.	Apoptosis			Necrosis %
	Total %	Early %	Late %	
T-1-MBHEPA	21.35	7.22	2.72	11.41
Control MCF7	3.06	0.71	0.13	2.22

4. Discussions

The DFT studies optimized the structure of **T-1-MBHEPA** and analyzed its charge distribution. The results revealed significant charge delocalization and potential reactivity. Computational analyses supported its flexibility and reactivity. Molecular ESP mapping highlighted regions open to electrophilic and nucleophilic attacks. The total density of states analysis showed occupied orbitals under HOMO. QTAIM analysis provided insights into electron density and bonding. These findings enhance our understanding of **T-1-MBHEPA**'s reactivity and general bonding potential.

The molecular docking findings suggested powerful VEGFR-2 inhibitory actions of **T-1-MBHEPA** through the correct binding and the various interactions. Moreover, MD simulations provided further validation of the precise binding interaction between **T-1-MBHEPA** and

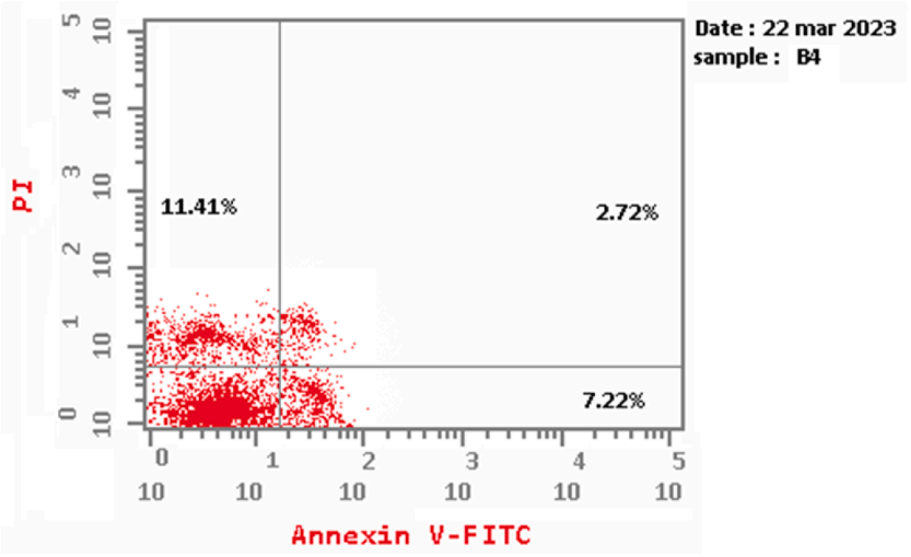

Fig. 11. Flow cytometric chart of apoptosis in MCF7 cells exposed to **T-1-MBHEPA.**

Table 4
The effect of **T-1-MCPAB** on MCF7′s migration and healing after 48 h.

	at 0 h		at 48 h		RM um	Wound closure % um^2	Area difference %
	area	width	area	width			
Control cells	1000.333	999.385	340.500	339.538	13.746	65.961	659.833
T-1-MBHEPA	964.000	963.044	892.6667	891.751	1.485	7.399	71.333

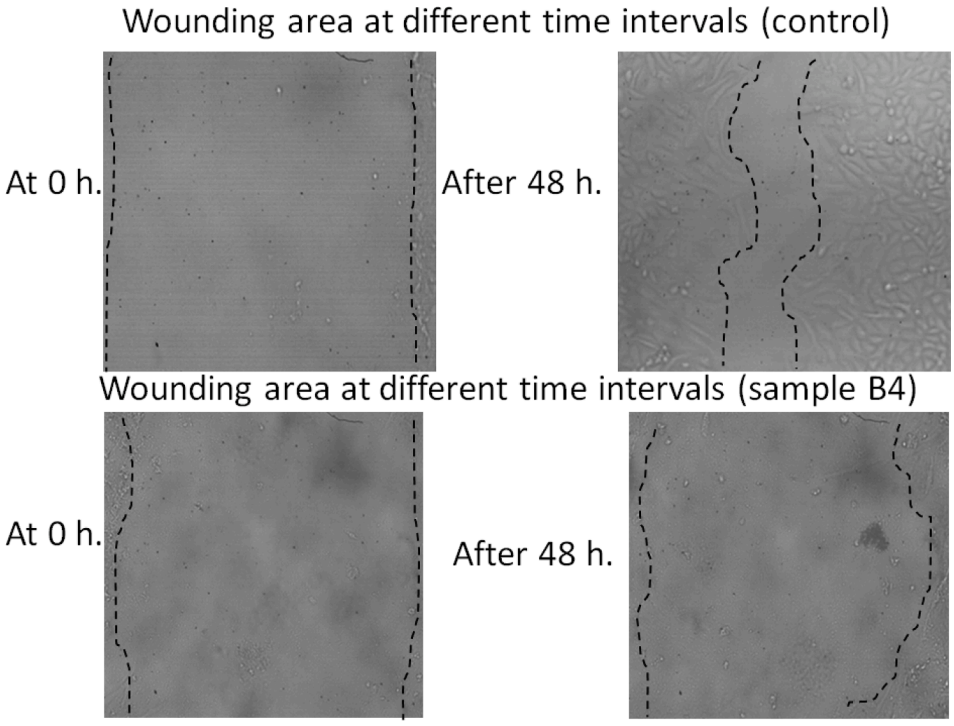

Fig. 12. The effect of **T-1-MBHEPA** on MCF7′s migration and healing potential after 48 h.

VEGFR-2, demonstrating a sustained conformation and stable proximity to the center of mass of VEGFR-2. The small RMSD values reached an equilibrium at approximately 2.7 Å for the apo protein and 2.1 Å for the holo protein, indicating a robust structural stability. Radius of gyration and solvent-accessible surface area analyses lent additional support to the overall structural integrity. The elevated hydrogen bond count remained consistently at 70 bonds, underscoring the persistence of critical interactions. While most amino acids exhibited steadfast stability, minor fluctuations were observed in specific regions, suggesting localized flexibility.

Moving forward, the MM-GBSA analysis unraveled a highly favorable binding interaction, characterized by a substantial binding energy of −41 kcal/mol. This strong affinity was primarily attributed to van der Waals interactions, emphasizing the role of non-covalent forces in stabilizing the complex. Notably, the specific key amino acid contributors to the binding energy, were determined. Furthermore, the three-dimensional binding conformations were meticulously extracted through the PLIP analysis, providing invaluable insights into the detailed intermolecular interactions between **T-1-MBHEPA** and VEGFR-2. This comprehensive computational analysis underscores the robust and stable nature of the binding interaction, affirming the potential of **T-1-MBHEPA** as a potent VEGFR-2 inhibitor. Based on the ADMET prediction, it can be inferred that **T-1-MBHEPA** possesses a favorable pharmacokinetic profile which is crucial as it ensures optimal bioavailability and sustained activity at the target site. As well as it was anticipated to be safe in 8 different toxicity models.

The alignment between our *in silico*, *in vitro*, and *in vivo* results underscores the potential of **T-1-MBHEPA** as a promising candidate for cancer treatment. Following its semi-synthesis, which was meticulously confirmed through a series of spectroscopic analyses, our *in vitro* studies unveiled compelling evidence of **T-1-MBHEPA**'s remarkable inhibitory effects on VEGFR-2, with IC50 values of 1.214 μg/mL. **T-1-MBHEPA**'s selectivity against VEGFR-2 was confirmed as it didn't show promising activity against EGFR and PDGFRβ kinases Validating the obtained *in silico* results and highlighting its potent anti-angiogenic properties, crucial for impeding tumor angiogenesis. Furthermore, the strong activity with selectivity values of 16 and 17 against the HepG2 and MCF7 cancer cell lines, respectively, emphasize **T-1-MBHEPA**'s specificity towards cancer cells, affirming its potential as a targeted therapeutic agent.

In addition to its anti-VEGFR-2 properties, **T-1-MBHEPA** exhibited other favorable characteristics in our *in vitro* studies. It triggered apoptosis, signaling its capacity to induce self-destruction among cancer cells. Moreover, **T-1-MBHEPA** demonstrated the ability to inhibit the production of interleukin-2 (IL-2) and tumor necrosis factor alpha (TNFα), two inflammatory cytokines implicated in cancer progression. By curbing the release of these cytokines, T-1-MBHEPA holds promise for mitigating cancer-related inflammation and its associated detrimental effects.

Our studies also shed light on **T-1-MBHEPA**'s potential to impede the healing and migration of MCF7 cells, a crucial attribute in the context of breast cancer. Disrupting these vital cellular processes can effectively curtail the metastatic potential of cancer cells, contributing to the containment of tumor growth and spread.

Moreover, our *in vivo* assessments revealed that **T-1-MBHEPA**'s oral administration did not result in liver function (ALT and AST) or kidney function (creatinine and urea) toxicity in mice. These findings were harmonized with the *in silico* ADMET and toxicity results underscoring **T-1-MBHEPA**'s safety profile and positioning it as a well-tolerated candidate for further investigation.

5. Conclusion

In summary, (**T-1-MCPAB**), is a semisynthetic theobromine derivative designed to inhibit VEGFR-2 protein based on VEGFR-2 inhibitors' essential structural properties. Its ability to inhibit VEGFR-2 was confirmed by molecular docking and six MDs (over 100 ns), MM-GBSA, PLIP, essential dynamics, and three DFT experiments. Furthermore, the ADMET analysis revealed that this compound was drug-like and likely safe based on its similarity to **T-1-MCPAB**. Following semi-synthesis, the *in vitro* studies showed that **T-1-MBHEPA** significantly inhibits VEGFR-2 with IC_{50} values of 1.214 μg/mL, with selectivity values of 4.61 and 4.85 against two cancer cell lines HepG2 and MCF7 respectively. It also triggered apoptosis and prevented IL-2 and TNFα in addition to its potential to prevent MCF7′s healing and migration. *In vivo*, **T-1-MBHEPA** showed no liver (ALT and AST) or kidney (creatinine and urea) toxicity, affirming its safety and aligning with *in silico* ADMET and toxicity results. These findings hint at a promising future prospective for **T-1-MBHEPA** as a lead tolerable compound in further research towards breast cancer treatment.

Availability of data and material

All data regarding this work were mentioned in the manuscript and the supplementary data. **T-1-MBHEPA** is available from the authors upon request.

Funding

This research was funded by Princess Nourah bint Abdulrahman University Researchers Supporting Project number (PNURSP2023R116), Princess Nourah bint Abdulrahman University, Riyadh, Saudi Arabia.

Authors' contributions

The conception, design, and supervision of the study were undertaken by IHE and AMM. The semisynthesis was conducted by RGY and HE, while DZH, HE, EBK, and IMI performed the computational studies. MAA took on the responsibility of writing, analyzing, and interpreting the data. MAE performed the *in vivo* studies.The funding for the study was acquired by EBE and AAA, who were also involved in the manuscript writing process. All authors have diligently reviewed and reached a consensus on the final version of the manuscript.

Declaration of competing interest

The authors declare that they have no known competing financial interests or personal relationships that could have appeared to influence the work reported in this paper.

Acknowledgement

The authors extend their appreciation to the Research Center at AlMaarefa University for funding this work.

Appendix A. Supplementary material

Supplementary data to this article can be found online at https://doi.org/10.1016/j.jsps.2023.101852.

References

Alanazi, M.M., Eissa, I.H., Alsaif, N.A., et al., 2021. Design, synthesis, docking, ADMET studies, and anticancer evaluation of new 3-methylquinoxaline derivatives as VEGFR-2 inhibitors and apoptosis inducers. J. Enzyme Inhib. Med. Chem. 36, 1760–1782.

Ali, S., M. I. Ullah, A. Sajjad, et al., 2021. Environmental and health effects of pesticide residues. Sustainable Agriculture Reviews 48: Pesticide Occurrence, Analysis and Remediation Vol. 2 Analysis. 311-336.

Alley, M.C., Scudiero, D.A., Monks, A., et al., 1988. Feasibility of drug screening with panels of human tumor cell lines using a microculture tetrazolium assay. Cancer Res. 48, 589–601.

Amadei, A., A. B. Linssen, H. J. J. P. S. Berendsen, Function,, et al., 1993. Essential dynamics of proteins. 17, 412-425.

Angelo, L.S., Kurzrock, R., 2007. Vascular endothelial growth factor and its relationship to inflammatory mediators. Clin. Cancer Res. 13, 2825–2830.

Bai, J., Wu, J., Tang, R., et al., 2020. Emodin, a natural anthraquinone, suppresses liver cancer in vitro and in vivo by regulating VEGFR 2 and miR-34a. Invest. New Drugs 38, 229–245.

Chinedu, E., Arome, D., Ameh, F.S., 2013. A new method for determining acute toxicity in animal models. Toxicol. Int. 20, 224.

del Carmen Quintal Bojórquez, N. and M. R. Campos, 2023. Traditional and Novel Computer-Aided Drug Design (CADD) Approaches in the Anticancer Drug Discovery Process. Current Cancer Drug Targets. 23, 333-345.

Dietrich, J., Hulme, C., Hurley, L.H., 2010. The design, synthesis, and evaluation of 8 hybrid DFG-out allosteric kinase inhibitors: A structural analysis of the binding

interactions of Gleevec®, Nexavar®, and BIRB-796. Bioorg. Med. Chem. 18, 5738–5748.
Elkady, H., Elwan, A., El-Mahdy, H.A., et al., 2022. New benzoxazole derivatives as potential VEGFR-2 inhibitors and apoptosis inducers: Design, synthesis, anti-proliferative evaluation, flowcytometric analysis, and in silico studies. J. Enzyme Inhib. Med. Chem. 37, 403–416.
Elkady, H., Abuelkhir, A.A., Rashed, M., et al., 2023. New thiazolidine-2, 4-diones as effective anti-proliferative and anti-VEGFR-2 agents: Design, synthesis, in vitro, docking, MD simulations, DFT, ADMET, and toxicity studies. Comput. Biol. Chem. 107, 107958.
Elkady, H., El-Dardir, O.A., Elwan, A., et al., 2023. Synthesis, biological evaluation and computer-aided discovery of new thiazolidine-2, 4-dione derivatives as potential antitumor VEGFR-2 inhibitors. RSC Adv. 13, 27801–27827.
Elkaeed, E.B., Taghour, M.S., Mahdy, H.A., et al., 2022. New quinoline and isatin derivatives as apoptotic VEGFR-2 inhibitors: design, synthesis, anti-proliferative activity, docking, ADMET, toxicity, and MD simulation studies. J. Enzyme Inhib. Med. Chem. 37, 2191–2205.
Elkaeed, E.B., Yousef, R.G., Elkady, H., et al., 2022. In silico, in vitro VEGFR-2 inhibition, and anticancer activity of a 3-(hydrazonomethyl) naphthalene-2-ol derivative. J. Biomol. Struct. Dyn. 1–16.
Elkaeed, E.B., Yousef, R.G., Elkady, H., et al., 2022. Design, synthesis, docking, DFT, MD simulation studies of a new nicotinamide-based derivative: In vitro anticancer and VEGFR-2 inhibitory effects. Molecules 27, 4606.
Elkaeed, E.B., Eissa, I.H., Elkady, H., et al., 2022. A multistage in silico study of natural potential inhibitors targeting SARS-CoV-2 main protease. Int. J. Mol. Sci. 23, 8407.
Elkaeed, E. B., R. G. Yousef, H. Elkady, et al., 2022. Design, Synthesis, Docking, DFT, MD Simulation Studies of a New Nicotinamide-Based Derivative: In Vitro Anticancer and VEGFR-2 Inhibitory Effects. Molecules. 27, 4606.
Elkaeed, E. B., R. G. Yousef, H. Elkady, et al., 2022. The Assessment of Anticancer and VEGFR-2 Inhibitory Activities of a New 1 H-Indole Derivative: In Silico and In Vitro Approaches. Processes. 10, 1391.
Elkaeed, E.B., Youssef, F.S., Eissa, I.H., et al., 2022. Multi-step in silico discovery of natural drugs against COVID-19 targeting main protease. Int. J. Mol. Sci. 23, 6912.
Elton, D.C., Boukouvalas, Z., Fuge, M.D., et al., 2019. Deep learning for molecular design—a review of the state of the art. Mol. Syst. Des. Eng. 4, 828–849.
Elwan, A., Abdallah, A.E., Mahdy, H.A., et al., 2022. Modified benzoxazole-based VEGFR-2 inhibitors and apoptosis inducers: Design, synthesis, and anti-proliferative evaluation. Molecules 27, 5047.
Erdem, L., Giovannetti, E., Leon, L.G., et al., 2012. Polymorphisms to predict outcome to the tyrosine kinase inhibitors gefitinib, erlotinib, sorafenib and sunitinib. Curr. Top. Med. Chem. 12, 1649–1659. https://doi.org/10.2174/156802612803531333.
Fan, J., Fu, A., Zhang, L., 2019. Progress in molecular docking. Quant. Biol. 7, 83–89.
Fathi Maroufi, N., Taefehshokr, S., Rashidi, M.-R., et al., 2020. Vascular mimicry: changing the therapeutic paradigms in cancer. Mol. Biol. Rep. 47, 4749–4765.
Ferreira, L.L., Andricopulo, A.D., 2019. ADMET modeling approaches in drug discovery. Drug Discov. Today 24, 1157–1165.
Fontanella, C., Ongaro, E., Bolzonello, S., et al., 2014. Clinical advances in the development of novel VEGFR2 inhibitors. Ann. Transl. Med. 2, 123. https://doi.org/10.3978/j.issn.2305-5839.2014.08.14.
Fujita, K.I., Ishida, H., Kubota, Y., et al., 2017. Toxicities of receptor tyrosine kinase inhibitors in cancer pharmacotherapy: Management with clinical pharmacology. Curr. Drug Metab. 18, 186–198. https://doi.org/10.2174/1389200218666170105165832.
Hartmann, J.T., Haap, M., Kopp, H.G., et al., 2009. Tyrosine kinase inhibitors - a review on pharmacology, metabolism and side effects. Curr. Drug Metab. 10, 470–481. https://doi.org/10.2174/138920009788897975.
Huang, L., Huang, Z., Bai, Z., et al., 2012. Development and strategies of VEGFR-2/KDR inhibitors. Future Med. Chem. 4, 1839–1852.
Huillard, O., Boissier, E., Blanchet, B., et al., 2014. Drug safety evaluation of sorafenib for treatment of solid tumors: consequences for the risk assessment and management of cancer patients. Expert Opin. Drug Saf. 13, 663–673. https://doi.org/10.1517/14740338.2014.907270.
Idakwo, G., Luttrell, J., Chen, M., et al., 2018. A review on machine learning methods for in silico toxicity prediction. J. Environ. Sci. Health C Environ. Carcinog. Ecotoxicol. Rev. 36, 169–191. https://doi.org/10.1080/10590501.2018.1537118.
Jonkman, J.E., Cathcart, J.A., Xu, F., et al., 2014. An introduction to the wound healing assay using live-cell microscopy. Cell Adh. Migr. 8, 440–451.
Kataoka, Y., Mukohara, T., Tomioka, H., et al., 2012. Foretinib (GSK1363089), a multi-kinase inhibitor of MET and VEGFRs, inhibits growth of gastric cancer cell lines by blocking inter-receptor tyrosine kinase networks. Invest. New Drugs 30, 1352–1360.
Kinnings, S.L., Jackson, R.M., 2009. Binding site similarity analysis for the functional classification of the protein kinase family. J. Chem. Inf. Model. 49, 318–329.
Kruhlak, N.L., Benz, R.D., Zhou, H., et al., 2012. (Q)SAR modeling and safety assessment in regulatory review. Clin. Pharmacol. Ther. 91, 529–534. https://doi.org/10.1038/clpt.2011.300.
Levy, A., Benmoussa, L., Ammari, S., et al., 2014. Reversible posterior leukoencephalopathy syndrome induced by axitinib. Clin. Genitourin. Cancer 12, e33–e34. https://doi.org/10.1016/j.clgc.2013.08.008.
Li, X., Chai, J., Wang, Z., et al., 2018. Reversible posterior leukoencephalopathy syndrome induced by apatinib: a case report and literature review. OncoTargets Ther. 11, 4407–4411. https://doi.org/10.2147/ott.S166605.
Lugano, R., Ramachandran, M., Dimberg, A., 2020. Tumor angiogenesis: causes, consequences, challenges and opportunities. Cell. Mol. Life Sci. 77, 1745–1770.
Luo, G., Li, X., Zhang, G., et al., 2017. Novel SERMs based on 3-aryl-4-aryloxy-2H-chromen-2-one skeleton-A possible way to dual ERα/VEGFR-2 ligands for treatment of breast cancer. Eur. J. Med. Chem. 140, 252–273.
Machado, V.A., Peixoto, D., Costa, R., et al., 2015. Synthesis, antiangiogenesis evaluation and molecular docking studies of 1-aryl-3-[(thieno [3, 2-b] pyridin-7-ylthio) phenyl] ureas: Discovery of a new substitution pattern for type II VEGFR-2 Tyr kinase inhibitors. Bioorg. Med. Chem. 23, 6497–6509.
Modi, S.J., Kulkarni, V.M., 2019. Vascular endothelial growth factor receptor (VEGFR-2)/KDR inhibitors: medicinal chemistry perspective. Med. Drug Discov. 2, 100009.
Moradi, M., Mousavi, A., Emamgholipour, Z., et al., 2023. Quinazoline-based VEGFR-2 inhibitors as potential anti-angiogenic agents: A contemporary perspective of SAR and molecular docking studies. Eur. J. Med. Chem., 115626
Nascimento, I. J. d. S., T. M. de Aquino and E. F. da Silva-Júnior, 2022. The new era of drug discovery: The power of computer-aided drug design (CADD). Letters in Drug Design & Discovery. 19, 951-955.
NDC, Q. B. and M. Campos, 2022. Traditional and Novel Computer-Aided Drug Design (CADD) Approaches in the Anticancer Drug Discovery Process Computer-Aided Drug Design (CADD) Approaches in the Development of Anticancer Drugs. Current Cancer Drug Targets.
Obot, I., Macdonald, D., Gasem, Z., 2015. Density functional theory (DFT) as a powerful tool for designing new organic corrosion inhibitors. Part 1: an overview. Corros. Sci. 99, 1–30.
Ou, X.-M., Li, W.-C., Liu, D.-S., et al., 2009. VEGFR-2 antagonist SU5416 attenuates bleomycin-induced pulmonary fibrosis in mice. Int. Immunopharmacol. 9, 70–79.
Papaleo, E., P. Mereghetti, P. Fantucci, et al., 2009. Free-energy landscape, principal component analysis, and structural clustering to identify representative conformations from molecular dynamics simulations: the myoglobin case. 27, 889-899.
Reker, D., Schneider, G., 2015. Active-learning strategies in computer-assisted drug discovery. Drug Discov. Today 20, 458–465.
Rodriguez, L. G., X. Wu and J.-L. Guan, 2005. Wound-healing assay. Cell Migration: Developmental Methods and Protocols. 23-29.
Schmidt, S., Gonzalez, D., Derendorf, H., 2010. Significance of protein binding in pharmacokinetics and pharmacodynamics. J. Pharm. Sci. 99, 1107–1122.
Shacter, E. and S. A. Weitzman, 2002. Chronic inflammation and cancer. Oncology (Williston Park, NY). 16, 217-226, 229; discussion 230.
Shah, A.A., Kamal, M.A., Akhtar, S., 2021. Tumor angiogenesis and VEGFR-2: mechanism, pathways and current biological therapeutic interventions. Curr. Drug Metab. 22, 50–59.
Shi, L., Zhou, J., Wu, J., et al., 2016. Anti-angiogenic therapy: Strategies to develop potent VEGFR-2 tyrosine kinase inhibitors and future prospect. Curr. Med. Chem. 23, 1000–1040.
Sivaraj, K.K., Takefuji, M., Schmidt, I., et al., 2013. G13 controls angiogenesis through regulation of VEGFR-2 expression. Dev. Cell 25, 427–434.
Spannuth, W.A., Nick, A.M., Jennings, N.B., et al., 2009. Functional significance of VEGFR-2 on ovarian cancer cells. Int. J. Cancer 124, 1045–1053.
Taghour, M.S., Elkady, H., Eldehna, W.M., et al., 2022. Discovery of new quinoline and isatine derivatives as potential VEGFR-2 inhibitors: design, synthesis, antiproliferative, docking and MD simulation studies. J. Biomol. Struct. Dyn. 1–16.
Taghour, M.S., Elkady, H., Eldehna, W.M., et al., 2022. Design, synthesis, anti-proliferative evaluation, docking, and MD simulations studies of new thiazolidine-2, 4-diones targeting VEGFR-2 and apoptosis pathway. PLoS One 17, e0272362.
Taghour, M.S., Elkady, H., Eldehna, W.M., et al., 2022. Design and synthesis of thiazolidine-2, 4-diones hybrids with 1, 2-dihydroquinolones and 2-oxindoles as potential VEGFR-2 inhibitors: In-vitro anticancer evaluation and in-silico studies. J. Enzyme Inhib. Med. Chem. 37, 1903–1917.
Tesařová, P., Tesař, V., 2013. Proteinuria and hypertension in patients treated with inhibitors of the VEGF signalling pathway–incidence, mechanisms and management. Folia Biol. 59, 15–25.
Thakur, M. and D. Pathania, 2020. Environmental fate of organic pollutants and effect on human health. Abatement of Environmental Pollutants, Elsevier: 245-262.
Tian, S., Quan, H., Xie, C., et al., 2011. YN968D1 is a novel and selective inhibitor of vascular endothelial growth factor receptor-2 tyrosine kinase with potent activity in vitro and in vivo. Cancer Sci. 102, 1374–1380.
Van de Loosdrecht, A., R. Beelen, g. Ossenkoppele, et al., 1994. A tetrazolium-based colorimetric MTT assay to quantitate human monocyte mediated cytotoxicity against leukemic cells from cell lines and patients with acute myeloid leukemia. Journal of immunological methods. 174, 311-320.
Wang, X., Bove, A.M., Simone, G., et al., 2020. Molecular bases of VEGFR-2-mediated physiological function and pathological role. Front. Cell Dev. Biol. 8, 599281.
Wang, T., Husein, D.Z., 2023. Novel synthesis of multicomponent porous nano-hybrid composite, theoretical investigation using DFT and dye adsorption applications: Disposing of waste with waste. Environ. Sci. Pollut. Res. 30, 8928–8955.
Wang, Z., Wang, N., Han, S., et al., 2013. Dietary compound isoliquiritigenin inhibits breast cancer neoangiogenesis via VEGF/VEGFR-2 signaling pathway. PLoS One 8, e68566.
Yan, J.-D., Liu, Y., Zhang, Z.-Y., et al., 2015. Expression and prognostic significance of VEGFR-2 in breast cancer. Pathol.-Res. Pract. 211, 539–543.
Yang, X., Wang, Y., Byrne, R., et al., 2019. Concepts of artificial intelligence for computer-assisted drug discovery. Chem. Rev. 119, 10520–10594.
Yousef, R.G., Elkady, H., Elkaeed, E.B., et al., 2022. (E)-N-(3-(1-(2-(4-(2, 2, 2-Trifluoroacetamido) benzoyl) hydrazono) ethyl) phenyl) nicotinamide: A novel pyridine derivative for inhibiting vascular endothelial growth factor receptor-2: Synthesis, computational, and anticancer studies. Molecules 27, 7719.
Yousef, R.G., Elwan, A., Gobaara, I.M., et al., 2022. Anti-cancer and immunomodulatory evaluation of new nicotinamide derivatives as potential VEGFR-2 inhibitors and

apoptosis inducers: in vitro and in silico studies. J. Enzyme Inhib. Med. Chem. 37, 2206–2222.

Zhang, Y., X. Ding, C. Miao, et al., 2019. Propofol attenuated TNF-α-modulated occludin expression by inhibiting Hif-1α/VEGF/VEGFR-2/ERK signaling pathway in hCMEC/D3 cells. 19, 1-11.

Zhu, H. and B. I. Rini, 2015. Third-Generation TKIs (Axitinib, Tivozanib) in RCC: Enhanced Efficacy and Diminished Toxicity? Renal Cell Carcinoma: Molecular Targets and Clinical Applications. 217-236.